JCTC Journal of Chemical Theory and Computation

Computational Improvements to Quantum Wave Packet ab Initio Molecular Dynamics Using a Potential-Adapted, Time-Dependent Deterministic Sampling Technique

Jacek Jakowski, Isaiah Sumner, and Srinivasan S. Iyengar*

Departments of Chemistry and Physics, Indiana University, 800 E. Kirkwood Avenue, Bloomington, Indiana 47405

Received April 9, 2006

Abstract: In a recent publication, we introduced a computational approach to treat the simultaneous dynamics of electrons and nuclei. The method is based on a synergy between quantum wave packet dynamics and ab initio molecular dynamics. Atom-centered density-matrix propagation or Born−Oppenheimer dynamics can be used to perform ab initio dynamics. In this paper, wave packet dynamics is conducted using a three-dimensional direct product implementation of the distributed approximating functional free-propagator. A fundamental computational difficulty in this approach is that the interaction potential between the two components of the methodology needs to be calculated frequently. Here, we overcome this problem through the use of a time-dependent deterministic sampling measure that predicts, at every step of the dynamics, regions of the potential which are important. The algorithm, when combined with an on-the-fly interpolation scheme, allows us to determine the quantum dynamical interaction potential and gradients at every dynamics step in an extremely efficient manner. Numerical demonstrations of our sampling algorithm are provided through several examples arranged in a cascading level of complexity. Starting from a simple one-dimensional quantum dynamical treatment of the shared proton in $[Cl-H-Cl]^-$ and $[CH_3-H-Cl]^-$ along with simultaneous dynamical treatment of the electrons and classical nuclei, through a complete three-dimensional treatment of the shared proton in $[Cl-H-Cl]^-$ as well as treatment of a hydrogen atom undergoing donor−acceptor transitions in the biological enzyme, soybean lipoxygenase-1 (SLO-1), we benchmark the algorithm thoroughly. Apart from computing various error estimates, we also compare vibrational density of states, inclusive of full quantum effects from the shared proton, using a novel unified velocity−velocity, flux−flux autocorrelation function. In all cases, the potential-adapted, time-dependent sampling procedure is seen to improve the computational scheme tremendously (by orders of magnitude) with minimal loss of accuracy.

Introduction

The time-dependent Schrödinger equation is a starting point for several dynamical methodologies in gas-phase[1] and condensed-phase quantum mechanics.[2] The Born−Oppenheimer approximation, when invoked, allows for separation of electronic and nuclear degrees of freedom and the subsequent propagation of nuclei, quantum-mechanically,[1,3−27] classically,[28−32] or semiclassically[33−48] on fitted electronic surfaces or "on-the-fly"[28−33,40−43,49−51] approximations to the same. For cases where fitted electronic surfaces are used, the required number of quantum chemical calculations to obtain a representation of the surface can be large depending upon the size of the system. It is in this regard that "on-the-fly" approaches to dynamics of nuclei and electrons[28−33,40−43,49−51] have recently become popular, leading to the subfield of ab initio molecular dynamics (AIMD).

In AIMD, an approximation to the electronic wave function is propagated along with the nuclear degrees of freedom to simulate dynamics on the Born−Oppenheimer surface. AIMD approaches can be broadly categorized as

* Corresponding author e-mail: iyengar@indiana.edu.

10.1021/ct600131g CCC: $33.50
Published on Web 08/17/2006

(a) Born−Oppenheimer molecular dynamics approaches, where the electronic degrees of freedom are represented using self-consistently converged electronic structure calculations (at the level of density functional theory, Hartree−Fock, post-Hartree−Fock or semiempirical methods) or (b) extended Lagrangian approaches,[52,53] where an approximation to the electronic structure is propagated through an adjustment of the relative time-scales of electrons and nuclei.[30,32,50,54,55] The AIMD approaches, when combined with full quantum or semiclassical dynamics schemes, have the potential to treat large problems accurately with the complete machinery of quantum dynamics. Several steps have been taken in this direction both for real and imaginary time quantum propagation.[33,42,56−60]

We have recently developed an approach[59,60] that attempts to overcome some computational bottlenecks in this area. Our approach is quantum-classical[39,61−67] and combines quantum-wave packet dynamics treatment of the time-dependent Schrödinger equation with ab initio molecular dynamics (where the nuclei are treated classical). The latter can be performed using Atom-centered Density-Matrix Propagation (ADMP)[32,55] or Born−Oppenheimer molecular dynamics (BOMD).[28,29,31] The wave packet dynamics is performed through an analytic, banded, Toeplitz representation to the discretized free propagator known as "distributed approximating functionals" (DAF).[27,68−72] [The (i,j)th element of a Toeplitz matrix depends only on $|i - j|$. This property of the free propagator used in the current contribution yields an efficient scheme where only the first (banded) row of the matrix representation of the time-evolution operator needs to be stored.] Some notable features of our wave packet AIMD approach are as follows: (a) The quantum dynamical free-propagation is formally exact and computationally efficient. It includes important quantum-effects such as zero-point effects, tunneling, and over-barrier reflections. (b) The electronic structure is simultaneously treated using hybrid density functionals (for example, B3LYP)[73−75] and derives its strength from established linear scaling electronic structure techniques.[76−78] (The computational complexity of the quantum dynamics formalism scales linearly with grid basis size.[59])

However, there remains an important computational difficulty in our approach.[59] An approximation to the time-dependent interaction potential between the quantum dynamical system and the AIMD system is required on the grid representation of the quantum wave packet, at every instant in time. If ab initio methods are used to represent the electronic degrees of freedom, this presents a major computational task and hinders the direct application of this methodology for higher dimensional quantum dynamical subsystems. We overcome this hurdle here by introducing a potential adapted time-dependent, deterministic sampling measure that allows us to only evaluate the time-dependent interaction potential in important regions. The sampling measure at any given step during the dynamics is cast as a function of the interaction potential, the gradients of the potential with respect to the quantum dynamical particle and wave packet amplitude, all of which are determined at the previous dynamics step.

The paper is organized as follows: For the convenience of the reader, the dynamics formalism is briefly reviewed in section 2. Details can be found in refs 59 and 60. The time-dependent deterministic sampling algorithm is briefly introduced toward the end of section 2 and discussed in more detail in sections 3 and 4. Appendices A−C facilitate this formal discussion. Numerical tests are presented in section 5 and include demonstrations of the computational improvement obtained from the sampling technique for quantum dynamical treatment of a single particle undergoing dynamics along with the surrounding electronic degrees of freedom and classical nuclear degrees of freedom. Examples include treatment of the single quantum particle in one dimension and in full three dimensions, and the systems studied involve hydrogen, hydride or proton-transfer processes in $[Cl-H-Cl]^-$, $[CH_3-H-Cl]^-$, and the biological enzyme, soybean lipoxygenase-1 (SLO-1). In all cases the computational improvements seen due to the use of time-dependent deterministic sampling are excellent. Our conclusions and outlook toward further improvements are presented in section 6.

II. A Quantum Wave Packet Generalization for ab Initio Molecular Dynamics

In this section we first summarize the governing equations of motion and approximations involved in the quantum wave packet ab initio dynamics formalism. (Further details can be found in refs 59 and 60.) We then proceed to highlight the main computational bottlenecks which form the basis for the rest of this paper.

To efficiently propagate an electron−nuclear system, we start from the time dependent Schrödinger equation (TDSE) and assume that, in large systems, some nuclei may require only classical treatment, but other parts of the system may need to be treated by applying quantum dynamics.[59,60] As a result, we partition the electron−nuclear system into separate, but interacting subsystems:[45−48] Subsystem 1 comprises particles that are treated quantum dynamically. Subsystem 2 contains the nuclei whose description will be given classically, and subsystem 3 comprises the electrons in the system. In the discussion below and the rest of this paper, we represent the position variables for the particles in subsystem 1 as R_{QM}. Similarly, the particles in subsystem 2 are represented using the position variables $\mathbf{R}_C$, and those in subsystem 3 are represented using r_e. We then invoke the time-dependent self-consistent field (TDSCF) mean field separation[45,46,61,79] wherein the full wave function is approximated as a product: $\psi(R_{QM}, \mathbf{R}_C, r_e; t) \equiv \psi_1(R_{QM})\psi_2(\mathbf{R}_C)\psi_3(r_e)\exp[\imath\gamma]$, and $\dot{\gamma}$ (that is the first time-derivative of γ) is proportional to twice the energy of the system. This leads to three separate time-dependent Schrödinger equations, one for each subsystem, and the Hamiltonian for each separate Schrödinger equation is mean-field and depends on the state of the other two subsystems, for example, $H_1 = \langle\psi_2\psi_3|\mathscr{H}|\psi_2\psi_3\rangle$. (See ref 59.)

In the next step we recognize that the particles in subsystem 1 are to be treated using quantum dynamics, and hence we retain the time-dependent Schrödinger equation for subsystem 1, following dynamics under the Hamiltonian

H_1. But, since subsystem 2 comprises nuclei that are not required to be treated within a quantum dynamical formalism (since they are not part of subsystem 1), we enforce the classical limit ($\hbar \rightarrow 0$)[68,64,66,67,80−87] for these particles. In subsystem 3 we choose to enforce the space-time separation of electrons to obtain a stationary state (Born−Oppenheimer) description of electrons. In this fashion we recover a formalism where a portion of the full system is treated using quantum dynamics, another portion of the system is treated classically, while a third portion (the electrons) is described within a stationary state approximation. The description of the electrons can be achieved using Hartree−Fock, DFT, semiempirical, or post-Hartree−Fock formalisms, and if any of the single particle descriptions are used (Hartree−Fock, DFT, or semiempirical), then the electronic subsystem obeys a self-consistent field (SCF) procedure which leads to a converged single particle electronic density matrix, $\mathbf{P}_C$. In this situation, the equations of motion for subsystems 1 and 2 are

$$\imath\hbar\frac{\partial}{\partial t}\chi(R_{QM};t) = \left[-\frac{\hbar^2}{2M_{QM}}\nabla^2_{R_{QM}} + E(\{\mathbf{R}_C, \mathbf{P}_C\}, R_{QM})\right] \times \chi(R_{QM}; t) \quad (1)$$

and

$$\mathbf{M}\frac{d^2\mathbf{R}_C}{dt^2} = -\left\langle \chi \left| \frac{\partial E(\{\mathbf{R}_C,\mathbf{P}_C\}, R_{QM})}{\partial \mathbf{R}_C}\right|_{\mathbf{P}_C} \chi \right\rangle \quad (2)$$

where $\chi(R_{QM}; t)$ represents the quantum dynamical wave packet, $\mathbf{M}$ denotes the classical nuclear masses, and M_{QM} denotes the mass of the quantum subsystem particle(s). As stated above the equation for $\mathbf{P}_C$ is a self-consistent field equation arising from the single particle methodology of choice. If post-Hartree−Fock treatments are used, then the energy functionals in eqs 1 and 2 are appropriately modified. Subsystem 2 experiences an "averaged" force[88] that depends on the instantaneous wave packet χ.

An alternative description is obtained by employing the recently developed Atom-centered Density Matrix Propagation (ADMP) formalism[32,55,87,89−92] for subsystems 2 and 3. To arrive at this step, we first note that classical dynamics of subsystem 2 and the simultaneous self-consistent treatment of electrons together comprise the now well-known ab initio molecular dynamics (AIMD) paradigm.[28−33,40,49−51,93] It has been noted that under conditions of "adiabatic control",[50,89,90,94] extended-Lagrangian formalisms[52,53] such as ADMP can provide dynamical results in good agreement with Born Oppenheimer dynamics and experiment.[89,95] When ADMP is used to describe the dynamics of the electrons, the equation of motion for subsystem 3 is

$$\underline{\mu}^{1/2}\frac{d^2\mathbf{P}_C}{dt^2}\underline{\mu}^{1/2} = -\left\langle \chi \left| \frac{\partial E(\{\mathbf{R}_C,\mathbf{P}_C\}, R_{QM})}{\partial \mathbf{P}_C}\right|_{\mathbf{R}_C} \chi \right\rangle - [\Lambda\mathbf{P}_C + \mathbf{P}_C\Lambda - \Lambda] \quad (3)$$

Here, $\underline{\mu}$ is a fictitious inertia tensor[32,55,89,90] describing the motion of $\mathbf{P}_C$, and Λ is a Lagrangian multiplier matrix used to impose N-representability of $\mathbf{P}_C$. The energy functional, $E(\{\mathbf{R}_C,\mathbf{P}_C\}, R_{QM})$, in eqs 3 and 2, is obtained from a density functional treatment (or any other single particle treatment) of the electrons. The equations of motion for subsystem 2 remain the same as in eq 2 apart from the fact that the forces used in ADMP are different from that in Born−Oppenheimer[32,90] through the inclusion of an additional term that depends on the commutator of the single-particle electronic Hamiltonian (or Fock matrix) and $\mathbf{P}_C$. The ADMP subsystem also experiences an "averaged" force similar to subsystem 2. This averaged force and the N-representability constraints propagate $\{\mathbf{R}_C, \mathbf{P}_C\}$ which in turn affects the energy $E(\{\mathbf{R}_C, \mathbf{P}_C\}, R_{QM})$ and determines the dynamics of χ. The system of eqs 1−3 are thus coupled and are solved simultaneously as a single initial value problem.

If Born−Oppenheimer (BO) dynamics is used to represent subsystems 2 and 3, eq 3 is substituted by SCF convergence of $\mathbf{P}_C$. As a result, there arises an important and subtle difference between the ADMP and BO wave packet implementations. In BO, the density matrix, $\mathbf{P}_C$, becomes a function of both $\mathbf{R}_C$ and R_{QM}, but in ADMP, $\mathbf{P}_C$ does not depend on R_{QM}; $\mathbf{P}_C$ only depends on the distribution of the wave packet, $\chi(R_{QM};t)$. Thus in ADMP, the dynamics of $\mathbf{P}_C$ is Ehrenfest-like, while this is not the case when BO is used for the dynamics of $\mathbf{R}_C$, $\mathbf{P}_C$ in conjunction with quantum dynamics. As a result, in ADMP the calculation of $E(\{\mathbf{R}_C, \mathbf{P}_C\}, R_{QM})$ for each additional grid point is simplified, since the terms that depend only on $\mathbf{P}_C$ (the two-electron integrals in the Fock matrix) do not need to be recomputed. This important and subtle difference will be benchmarked in future publications.

The time-evolution of χ, in the coordinate-representation, is approximated using the symmetric split operator[5,96−98]

$$\chi(R^i_{QM};t+\Delta t) = \sum_j \exp\left\{-\frac{\imath V(R^i_{QM})}{2\hbar}t\right\}\tilde{K}(R^i_{QM}, R^j_{QM}) \times \exp\left\{-\frac{\imath V(R^j_{QM})}{2\hbar}t\right\}\chi(R^j_{QM};t) \quad (4)$$

and the free-propagator, $\tilde{K}(R^i_{QM}, R^j_{QM})$, is represented using distributed approximating functionals (DAF):[59,60,68,70]

$$\tilde{K}(R^i_{QM}, R^j_{QM}) = \frac{1}{\sigma(0)}\exp\left\{-\frac{(R^i_{QM} - R^j_{QM})^2}{2\sigma(\Delta t_{QM})^2}\right\} \times \sum_{n=0}^{M/2}\left(\frac{\sigma(0)}{\sigma(\Delta t_{QM})}\right)^{2n+1}\left(\frac{-1}{4}\right)^n\frac{1}{n!}(2\tau)^{-1/2}H_{2n}\left(\frac{R^i_{QM} - R^j_{QM}}{\sqrt{2}\sigma(\Delta t_{QM})}\right) \quad (5)$$

In eq 5, H_{2n} are even order Hermite polynomials.[99] The structure $\tilde{K}(R^i_{QM}, R^j_{QM}) \equiv \tilde{K}(|R^i_{QM} - R^j_{QM}|)$, renders a great deal of efficiency to our quantum propagation as discussed in refs 27, 59, 60, and 70. The evolution of $\{\mathbf{R}_C, \mathbf{P}_C\}$ is based on the velocity Verlet integrator[100] as discussed in ref 59.

An important advantage of this dynamical procedure for $\{\chi(R_{QM};t);\mathbf{R}_C,\mathbf{P}_C\}$ is that there is no need to prepare the potential energy surface a priori, since the potential in eq 1 is obtained on-the-fly. However, the need to obtain an approximation to the energy and gradients, $\langle\chi|\partial E(\{\mathbf{R}_C,\mathbf{P}_C\},$

R_{QM})/$\partial \mathbf{R_C}|_{\mathbf{P_C}}|\chi\rangle$ and $\langle\chi|\partial E(\{\mathbf{R_C},\mathbf{P_C}\},R_{QM})/\partial \mathbf{P_C}|_{\mathbf{R_C}}|\chi\rangle$, at every time-step, also constitutes a computational bottleneck in the current procedure, and the complexity grows with the number of grid points defined as part of the quadrature scheme in eq 4. Hence, the number of grid points where the electronic structure energy and gradients are evaluated needs to be optimized. This should bring the overall scaling of the algorithm down from a dependence on the total number of quantum dynamical grid points to a small fraction where the electronic structure calculations are performed. In section III, we introduce a time-dependent deterministic sampling measure which helps us to predetermine the relevant regions of the potential where the energy and gradients are to be obtained; the values of these parameters in the other regions are obtained through an efficient interpolation scheme. This procedure greatly reduces the computational cost associated with the algorithm, as will be seen in section V.

III. Time-Dependent Deterministic Sampling of the Quantum Potential Surface

To maintain accuracy of the quantum propagation, it is desirable to have the discretized coordinate representation (or grid) cover a large area and assume that the wave packet vanishes outside the grid boundaries. [The boundary conditions used here are the standard Dirichlet type boundary conditions. One could also use Neumann boundary conditions to solve this problem, and this generalization to the methodology is currently in progress.[137]] The density of grid points is then required to be high enough in "important" regions so as to facilitate accurate evaluation of the wave packet. This, however, leads us to a computational bottleneck for an on-the-fly calculation of the electronic energy and gradients. Here, we aim to dynamically determine an optimal and adequate set of grid point locations where the electronic energy and gradients are to be evaluated such that the error in the quantum dynamics is minimal and controllable. We introduce a potential adapted, time-dependent, deterministic sampling measure for this purpose. The formal discussion on the sampling measure in section III and subsequent discussion of the algorithm in section IV are couched in one dimension. The numerical implementation of this methodology in higher dimensions for Cartesian-like grids is discussed in section IV B. Multidimensional benchmarks are provided in sections V B and V C.

Consider a uniformly spaced set of N_Q grid points in the closed interval [a, b]. The number N_Q could in principle be large and constitutes the set of points where quantum dynamical propagation is to be performed. Let N_E represent a subset of these N_Q grid points ($N_E \ll N_Q$) where the electronic structure energies and gradients are to be obtained. The location of these N_E points needs to be optimal and *determined dynamically*, so that the propagation error

$$\sigma_{N_E} = \frac{1}{T}\int_0^T \{||\chi_{ref}(t) - \chi_{N_E}(t)||_2\}^2 \mathrm{d}t \qquad (6)$$

is small for both ADMP and BO wave packet implementations. The quantity $||A||_2$ is the L^2 norm[101,102] of vector A, and χ_{ref} denotes the reference wave packet propagated on a potential energy surface determined by electronic structure evaluations on all N_Q uniformly spaced grid points. The function χ_{N_E} denotes the propagated wave packet on a surface obtained using potential and gradient evaluations only on the N_E, in general nonuniformly distributed, grid points. The potential values at the remaining ($N_Q - N_E$) grid points are to be obtained from a suitable interpolation scheme and used in the quantum propagation of χ_{N_E}. The quantity T in eq 6 is the total time of propagation.

To determine the position of the N_E grid points, we introduce a sampling function, $\omega_0(R_{QM})$, which represents the density of points where the ab initio potential is to be evaluated. While constructing $\omega_0(R_{QM})$, we assume that it depends on the density of the wave packet, $\rho(R_{QM}) \equiv |\chi(R_{QM})|^2$, the potential energy $E(\{\mathbf{R_C},\mathbf{P_C}\}, R_{QM})$, and the magnitude of the potential gradient $[\nabla_{R_{QM}}E]$. We define our sampling function $\omega_0(R_{QM})$ to be inversely proportional to the values of potential energy since, generally, wave packets favor spatial regions with lower potential energy. Similarly, requiring $\omega_0(R_{QM})$ to be directly proportional to the gradients of the potential energy helps to maintain accuracy of integration in areas of the grid where the potential energy changes rapidly.[103] We further assume that $\omega_0(R_{QM})$ is directly proportional to wave packet amplitude $\rho(R_{QM})$. Accordingly our proposed sampling function has the form

$$\omega_0(R_{QM}) \equiv \omega_0(R_{QM};I_V, I_{V'}, I_\chi) = \frac{f_\rho(R_{QM};I_\chi) f_{E'}(R_{QM};I_{V'})}{f_E(R_{QM};I_V)} \qquad (7)$$

where the parameters I_V, $I_{V'}$, and I_χ can take on any numerical value, and the functions f_ρ, $f_{E'}$, and f_E are accordingly defined as

$$f_Y(R_{QM};\, i) = \begin{cases} Y(R_{QM}) & \text{for } i < 0 \\ 1 & \text{for } i = 0 \\ Y(R_{QM}) - Y_{min} + \dfrac{(Y_{max} - Y_{min})}{i} & \text{for } i > 0 \end{cases} \qquad (8)$$

Here $Y(R_{QM})$ denotes the wave packet density $\rho(R_{QM})$, potential energy, or gradients. The quantities Y_{max} and Y_{min} denote the maximum and minimum values of Y on the grid. When the index, i, is zero, then f_Y becomes a uniform function independent of Y, and all grid points are considered equally important. When the index is less than zero, then the function $Y(x)$ is used as is in eq 7, and if the index is greater than zero, then $Y(x)$ is shifted as per eq 8. We further assume that ω_0 is L^1 normalized[101] according to

$$||\omega_0||_1 = \sum_{i=1}^{N_Q} \omega_0(R^i_{QM})\Delta R_{QM} = \int_a^b |\omega_0(x)|\, dx = 1 \qquad (9)$$

where $\{R^i_{QM}\}$ are a set of quantum grid points in the closed interval [a,b], $\Delta R_{QM} = (b - a)/N_Q$ and $||\cdots||_1$ defines the L^1-norm. This normalization, in conjunction with the last option in eq 8, is used to regulate the contributions of wave packet density, potential energy, and gradients to the sampling function. This aspect is clear from the fact that for $i > 0$

$$f_Y(R_{QM};\, i) = (Y_{max} - Y_{min})\left[\tilde{Y}(R_{QM}) + \frac{1}{i}\right] \qquad (10)$$

where $\tilde{Y}(R_{QM}) = (Y(R_{QM}) - Y_{min})/(Y_{max} - Y_{min})$ and hence

$0 \le \tilde{Y} \le 1$. Thus, for the case of $i > 0$, the normalization condition essentially reduces the sampling function to

$$\omega_0(R_{QM}) \propto \frac{[\tilde{\rho} + 1/I_\chi] \times [\tilde{E}' + 1/I_{V'}]}{\tilde{E} + 1/I_V} \tag{11}$$

where $\tilde{\rho}$, $\tilde{E}'$, and $\tilde{E}$ are each bounded by 1. The contributions from the wave packet, gradients, and energy are thus controlled to allow a flexible scheme to enhance accuracy and efficiency. The performance of eq 7 for various values of I_V, $I_{V'}$, and I_χ and different potentials is presented in section 5. Using the implementations of this approach described in section 4, we choose a set of N_E grid points [$N_E = \alpha N_Q$ and $\alpha \le 1$] where the potential and gradients are evaluated. These data are used in conjunction with an interpolation procedure (discussed in Appendix B) to perform quantum wave packet dynamics on a uniform grid comprising N_Q points.

The interpretation of $\omega_0(R_{QM})$ is such that large values of this quantity indicate regions on the grid where energy and gradient evaluations *should* be conducted accurately using electronic structure methods. When $\omega_0(R_{QM})$ is small, the accuracy of energy and gradients is not critical, and the value of the potential in such regions is obtained though interpolation. Additional interpretations that connect the sampling function in eq 7 to the Wentzel−Kramers−Brillouin (WKB)[80] semiclassical theory and also to Bohmian mechanics[80−87,104−108] are discussed in Appendix A.

IV. Algorithms and Prescriptions for Time-Dependent Deterministic Sampling

A. Conditions on $\omega_0(x)$: The Requirements for a Smooth Transformation. Two important challenges arise while deriving a stable, general, numerical algorithm to carry out grid sampling as per eq 7. Both challenges only arise when the fraction of grid points where electronic structure calculations are to be performed becomes large (i.e., when $\alpha \equiv N_E/N_Q$ is close to 1). While this is not the practically interesting limit, since it is desired that most dynamical calculations are performed for small α, the demand for a stable numerical algorithm requires that we analyze all regions of α, and this analysis is carried out in the current section (section IV A). The computational algorithm of wave packet ab initio dynamics inclusive of sampling is described in section IV B.

For suitably large α the following problems arise. (i) On account of a uniform grid implementation of eq 4 in the current work, the function $\omega_0(R_{QM})$ should tend to a uniform function as $\alpha \to 1$. That is the set of N_E grid points must coincide with the set of N_Q underlying grid points as $\alpha \to 1$. (ii) In general, for any specific grid discretization given by grid spacing ΔR_{QM} and for any normalized function in eq 9, values of $[N_E \omega_0(R_{QM}) \Delta R_{QM}]$ could be greater than 1 if α is large. [Note that $N_E \Delta R_{QM} \equiv (b - a)\alpha$.] This would imply that there is a need for more than one potential evaluation in the vicinity of the point R_{QM}, which is clearly impossible. The solutions to both of these challenges are discussed for the remaining portion of this section.

As we see below, the first problem above is trivially solved. The second problem, however, necessitates a modification of the sampling function. Consider a smooth transformation, $\omega_0(R_{QM}) \to \omega(R_{QM})$, that maintains the original functional form of $\omega(R_{QM}) \equiv \omega_0(R_{QM})$ for small values of α (the practically interesting case of $N_E \ll N_Q$) but allows $\omega(R_{QM})$ to smoothly approach a uniform distribution as $\alpha \to 1$:

(a) $\omega(R_{QM})$ tends to a uniform distribution as $N_E/N_Q \to 1$ and

(b) $\omega(R_{QM}) \to \omega_0(R_{QM})$ for $N_Q \gg N_E$.

If $\omega(R_{QM})$ is normalized and bounded according to

$$||\omega(R_{QM})||_1 = \sum_{i=1}^{N_Q} \omega(R^i_{QM}) \Delta R_{QM} = \int_a^b \omega(x) dx = 1 \tag{12}$$

$$||N_E \omega(R_{QM}) \Delta R_{QM}||_\infty = N_E \max_i |\omega(R^i_{QM}) \Delta R_{QM}| \le 1 \tag{13}$$

it follows from eq 13 that

$$||\omega(R_{QM})||_\infty \equiv \max_i |\omega(R^i_{QM})| \le \frac{1}{\alpha(b-a)} \equiv \alpha^* \tag{14}$$

where we have used $\Delta R_{QM} = (b - a)/N_Q$. Using eq 12 we have

$$1 = \int_a^b \omega(x) dx \le (b-a) ||\omega(R_{QM})||_\infty \tag{15}$$

and thus

$$||\omega(R_{QM})||_\infty \ge \frac{1}{b-a} \tag{16}$$

Using eqs 14 and 16 we obtain upper and lower bounds to the L^∞ norm of $\omega(R_{QM})$ as

$$\frac{1}{(b-a)} \le ||\omega(R_{QM})||_\infty \le \frac{1}{\alpha(b-a)} \tag{17}$$

and hence

$$\lim_{\alpha \to 1} \omega(R^i_{QM}) = (b-a)^{-1} \tag{18}$$

Thus $\omega(R^i_{QM})$ tends to a uniform distribution in the limit $\alpha \to 1$, and condition (a) above is automatically satisfied from the requirements of eqs 12 and 13.

The second requirement, condition (b), is satisfied by introducing a smooth transformation that uses an additive correction function $U(R_{QM})$ to suitably compensate high-density regions (i.e., regions of $\omega_0(R_{QM})$ that are in violation of eq 13) of $\omega_0(R_{QM})$. Since this scheme has the physical effect of equalizing the sampling weights, it is referred to as the "spreading technique" and is the subject of the section below.

1. Smooth Transformation Spreading Technique. We now construct a spreading transformation to satisfy the condition (b) above, i.e., $\omega(R_{QM}) \to \omega_0(R_{QM})$ for $N_Q \gg N_E$. Let us start with a modification of $\omega_0(R_{QM})$ that satisfies eq 13. Toward this we construct two projection operators Ω_0 and Ω_0^c, such that

$$\Omega_0 f(x) = f(x) \cdot \theta[\omega_0(x) - \alpha^*] \tag{19}$$

where f is an arbitrary function defined in the closed interval

$[a, b]$, the quantity $\theta[\omega_0(x) - \alpha^*]$ is a Heaviside function that is equal to 1 when the argument in parentheses is greater than or equal to zero, and α^* is defined in eq 14. The operator Ω_0^c is the orthogonal complement of Ω_0 and is defined as

$$\Omega_0^c \; f(x) = f(x) \cdot \{1 - \theta[\omega_0(x) - \alpha^*]\} \tag{20}$$

The projection operators Ω_0 and Ω_0^c by definition exhaust the closed interval $[a, b]$, i.e.

$$I = \Omega_0 + \Omega_0^c \tag{21}$$

and I is the identity matrix.

If we assume a grid discretization comprising N_Q evenly spaced grid points in $[a, b]$, it is then our aim to obtain N_E optimally placed points as per the sampling function defined earlier. However, as a consequence of eqs 13 and 14 it follows that the operator Ω_0 represents a projection onto the region in space where $|N_E \omega_0(x) \mathrm{d}x| \equiv \omega_0(x)/\alpha^* \geq 1$. This is precisely the region where potential evaluations need to be performed. However, there is excess sampling density in this region which violates eq 13. This excess sampling density is exactly equal to $||\Omega_0 \tilde{\omega}_0||_1$, where $\tilde{\omega}_0 \equiv \{\omega_0(x) - \alpha^*\}$, and needs to be "spread" uniformly in the region represented by the projection operator Ω_0^c. To achieve this, we subtract this excess density from the regions belonging to Ω_0 and add this excess density *uniformly* to the region belonging to Ω_0^c. Consequently an additive correction to ω_0 is introduced

$$\omega_1 = \omega_0 + U(\omega_0) \tag{22}$$

where the additive spreading function $U(\omega_0)$ is defined as

$$U(\omega_0) = -\Omega_0 \tilde{\omega}_0 + \frac{||\Omega_0 \tilde{\omega}_0||_1}{||\{\Omega_0^c \mathbf{1}\}||_1} \{\Omega_0^c \mathbf{1}\} \tag{23}$$

Again, the first term of the above equation subtracts the excess density from the regions belonging to Ω_0. The second term adds this excess density *uniformly* to the region belonging to Ω_0^c. In the second term, the quantity $\{\Omega_0^c \mathbf{1}\}$ represents the projection of a constant vector $(\mathbf{1}(\mathbf{x}) \equiv 1$ for $x \in [a, b])$ onto the region belonging to Ω_0^c.

Equations 22 and 23 summarize the spreading technique. After applying the spreading transformation to $\omega_0(R_{QM})$, the excess sampling density described above is removed. However, in this process a similar excess density may be created in the region belonging to Ω_0^c. Thus, the sampling function ω_1 obtained from eq 22 may suffer the same way as ω_0 in the sense that there probably exists a finite region, $\Omega_1 \; f(x)$, on the grid:

$$\Omega_1 \; f(x) = f(x) \cdot \theta[\omega_1(x) - \alpha^*] \tag{24}$$

This implies that ω_1 does not satisfy eq 14 either. However, the excess density in the region represented by eq 24 is always smaller in magnitude than $||\Omega \tilde{\omega}_0||_1$ (see Appendix C for details on the convergence properties of the spreading technique) but still *needs to be spread again*. Consequently, the procedure described in eqs 22 and 23 is to be iterated according to

$$\omega_{i+1} = \omega_i + U(\omega_i) \tag{25}$$

where $U(\omega_i)$, as usual, corrects the excess density in ω_i:

$$U(\omega_i) = -\Omega_i \tilde{\omega}_i + \frac{||\Omega_i \tilde{\omega}_i||_1}{||\{\Omega_i^c \mathbf{1}\}||_1} \{\Omega_i^c \mathbf{1}\} \tag{26}$$

Hence, the generalized spreading transformation can be summarized using eqs 25 and 26 as

$$\begin{aligned} \omega_{i+1} &= \left(\Omega_i \alpha^* + \frac{||\Omega_i \tilde{\omega}_i||_1}{||\{\Omega_i^c \mathbf{1}\}||_1} \{\Omega_0^c \mathbf{1}\} \right) + \Omega_i^c \omega_i \\ &= \Omega_i \alpha^* + \Omega_i^c \left(\frac{||\Omega_i \tilde{\omega}_i||_1}{||\{\Omega_i^c \mathbf{1}\}||_1} + \omega_i \right) \end{aligned} \tag{27}$$

The convergence of this iterative technique is analyzed in Appendix C, and the scheme is shown to converge unconditionally.

It is further interesting to note that the procedure highlighted above, wherein the family of operators $\{\Omega_i\}$ and $\{\Omega_i^c\}$ modify the sampling function ω_0, has properties reminiscent of multiresolution analysis.[92,109−113] Our scheme, however, differs in that the *multiresolution* is based on spreading the "excess density" $||\Omega_0 \tilde{\omega}_0||_1$ as opposed to a translation-dilation process used in standard wavelet theory.

We now comment on the behavior of ω as $\alpha \rightarrow 0$. In this case the upper bound to $||\omega(R_{QM})||_\infty$ in eq 14 goes to infinity, and spreading is not required. Consequently, $\omega(R_{QM}) \rightarrow \omega_0(R_{QM})$ for $N_Q \gg N_E$ (condition (b) in section IV A). However, for values of α greater than zero, the spreading transformation enforces the condition in eq 14 as highlighted above.

B. Computational Implementation of Potential Adapted Time-Dependent Deterministic Sampling for Wave Packet ab Initio Molecular Dynamics. The algorithm to perform mixed quantum wave packet and ab initio dynamics (ADMP or BO) of the $\{\mathbf{R_C}, \mathbf{P_C}, \chi(\mathbf{R_{QM}})\}$ system, based on the sampling scheme, is outlined in this section.

As a preliminary step, a set of N_Q grid points, $\{\mathbf{R_{QM}^i}\}$, is created to represent the discretization of the quantum wave packet. The initial wave packet is defined on this grid. In our studies we have used (a) a real Gaussian function with width chosen such that the wave packet vanishes at the edges of the grid, (b) a thermally sampled linear combination of the eigenstates of the quantum Hamiltonian in eq 1 at $t = 0$, and (c) eigenstates of the quantum Hamiltonian in eq 1 at $t = 0$, as initial wave packets.

During each propagation cycle, the first step is to prepare a potential energy surface and corresponding gradients. The potential is used for quantum propagation, and the gradients are used to construct the AIMD forces (ADMP or BO) for propagation of the classical nuclei and electronic structure. The grid points where the potential and gradients are calculated is controlled by the sampling technique discussed earlier. Toward this, the sampling function is calculated based on the wave packet density, potential energy, and gradients of potential energy obtained from the previous step. [For the first wave packet AIMD step, the potential energy, gradients, and wave packet density are not available. Thus,

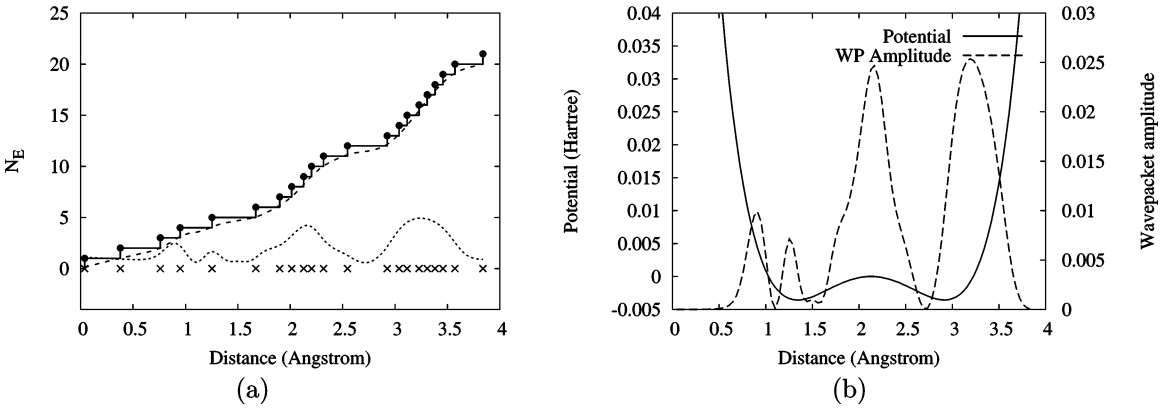

Figure 1. An illustration of the sampling function, $\omega(R_{QM})$, for $N_E = 21$ and $N_Q = 101$. Part (a) shows the sampling function (dotted line), its integral (dashed line), and ceiling function $\lceil \int_{x_0}^{x} dx' \omega(x') \rceil$. The 21 grid points are set at discontinuities of the ceiling function, and these points are represented in the figure using black dots on the discontinuous ceiling function and "X" at corresponding spots along the abscissa. Part (b) shows the corresponding potential surface and density of wave packet from which the sampling function is calculated.

the initial sampling function is chosen to be uniform.] The condition of eq 13 is then verified, and the iterative spreading scheme described in section IV A1 is applied to ω_0 if required. For small values of α ($\equiv N_E/N_Q$), spreading is generally not needed. Once the sampling function is determined based on the discussion in sections IV A, the grid points where the potential and gradients evaluations are to be conducted are determined based on the dimensionality of the grid as follows.

1. One-dimensional quantum propagation: The potential is sampled at grid points where the ceiling function $\lceil N_E \int_{x_0}^{x} dx' \omega(x') \rceil$ becomes discontinuous and is demonstrated in Figure 1. Here, $\lceil y \rceil$ represents the least integer greater than or equal to y and is called the ceiling of y. Accordingly, a grid map is created that describes the location of the N_E grid points where the potential energy and gradients are to be evaluated. This one-dimensional algorithm is used to obtain acceptable values of I_V, $I_{V'}$, and I_χ, to perform preliminary tests and also in the higher dimensional algorithm described below. The approach here has close connections to the theory of Haar wavelet transforms popular in digital signal processing.[76,92,109−115]

2. Quantum propagation in higher dimensions: There are in turn two options that we consider here. In one case, we construct reduced (or marginal) one-dimensional sampling functions according to

$$\omega_x(x) = \int \mathrm{d}y\mathrm{d}z\, \omega(x, y, z) \tag{28}$$

and similarly for $\omega_y(y)$ and $\omega_z(z)$. The sampling along each direction is then performed using the one-dimensional algorithm discussed above, and the overall grid is constructed as a direct sum. This algorithm is called marginal sampling in further discussion. The simplicity of this approach is appealing, and we find that the results obtained this way are sufficiently good as seen in sections V B and V C. A second algorithm that is more nonisotropic is as follows. The complete set of N_Q grid points are first partitioned into regular rectangular parallelepipeds (or cuboids) such that the integral of ω inside each parallelepiped is roughly a constant. This implies that each parallelepiped must contain the same number of sampling grid points, although their respective sizes may be different. If the number of sampling grid points inside each cuboid is chosen to be a small fraction of N_E, we may perform marginal sampling (eq 28) inside each parallelepiped. Both of these approaches constitute general schemes that we implement in arbitrary dimensions. The second scheme above, again, has strong connections to wavelet theory, and this aspect will be investigated as part of future publications.

Once the grid points are determined as above, the potential and gradients are computed, and the averaged AIMD forces in eqs 2 and 3 are updated. Since the wave packet is defined on the entire grid, while the potential and gradients are evaluated only on N_E grid points, estimation of the gradients on $[N_Q - N_E]$ grid points is required to calculate AIMD forces as per eqs 2 and 3. In this paper we have used a linear interpolation scheme to interpolate all gradients. The evaluated potential on the N_E grid points is used to obtain approximations to the potential energy at the remaining grid points using the Hermite curve interpolation scheme[116,117] described in Appendix B. For this $E(\{\mathbf{R_C},\mathbf{P_C}\}, R_{QM})$ and $\partial E(\{\mathbf{R_C},\mathbf{P_C}\}, R_{QM})/\partial \mathbf{R}_{QM}$ at all N_E grid points are used.

Next, the potential energy on the grid along with the DAF free propagator given by eq 5 are used for causal propagation of wave packet, $\chi(t)$, according to eq 4. The averaged energy gradients $\langle\chi(t)|\partial E(\{\mathbf{R_C},\mathbf{P_C}\},R_{QM})/\partial \mathbf{R_C}|\chi(t)\rangle$ and $\langle\chi(t)|\partial E(\{\mathbf{R_C},\mathbf{P_C}\},R_{QM})/\partial \mathbf{P_C}|\chi(t)\rangle$ are used to propagate $\mathbf{R_C}$ and $\mathbf{P_C}$. (The density matrix, $\mathbf{P_C}$, is obtained through SCF convergence for Born−Oppenheimer dynamics.) The next propagation cycle starts by calculating the sampling function and determining the grid positions for potential evaluation.

The propagation scheme has one additional feature that allows for further reduction in computational cost. As a preliminary step, the distance between all nuclei for all N_E grid points is calculated, and if any of these is found to be smaller than a fixed threshold, then the point is skipped during the potential and gradient evaluation and interpolated later. This aspect is similar to that used in the partial multidimensional grid method of Iordanov et al.,[118] where

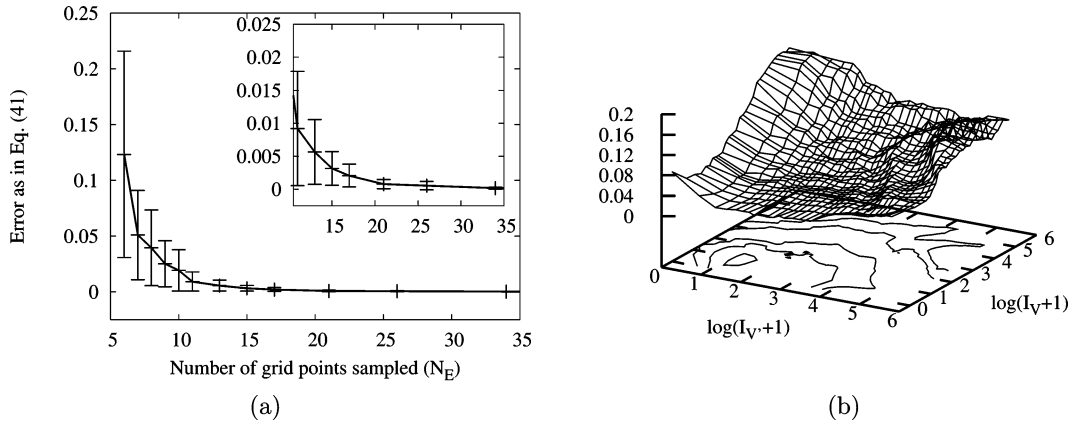

Figure 2. Part (a) shows the average error represented by eq 29 for $N_Q = 101$. Maximum deviations from the average error for individual potentials is displayed using the vertical error bars. As can be seen the error is negligible for all potentials beyond $N_E = 15$. Part (b) shows the behavior of σ_{av} in eq 30 as a function of I_V and $I_{V'}$. This part indicates that on average $I_V = 1$ and $I_{V'} = 3$ are a good choice.

the authors use a fixed energy cutoff based on short-range interaction between particles.

V. Numerical Results

In this section, we first obtain optimal values for sampling parameters I_V, $I_{V'}$, and I_χ described by eq 8. Our general idea toward this issue is to perform a multidimensional search in functional space to determine values of these parameters that would be optimal in an average sense. To simplify the problem, we first consider a series of one-dimensional potential energy functions and use these with the sampling measure to determine I_V and $I_{V'}$. (I_χ is set to zero for this portion of the parametrization.) These are then used to perform a series of quantum wave packet simulations in one dimension, and the accuracy of the dynamics is studied as a function of I_χ values. This helps to determine the value of all three parameters, and these calculations are described in section V A. A physical basis for the choice of I_V, $I_{V'}$, and I_χ is also provided at the end of section V A.

In sections V B and V C we use the parameters thus determined to (a) analyze the error in three-dimensional quantum dynamics for the $[Cl-H-Cl]^-$ system and a biological enzyme, soybean lipoxygenase-1 (SLO-1), and (b) to obtain a vibrational density of states inclusive of nuclear quantum effects. The density of states are obtained from a unified velocity−velocity, flux−flux autocorrelation function. We show that our sampling measure is very efficient in determining these spectra since small values of N_E are sufficient to determine the spectral data accurately.

A. Optimal Choice of I_V, I_V', and I_χ. To find optimal values for I_V and $I_{V'}$, 10 different model potentials were considered. The choice of these functions was based on their propensity to appear during molecular dynamics simulations. The potentials used in our tests are as follows:

1. Lennard-Jones 6−12 potential with coefficients $C_6 = C_{12} = 100$. The range of independent variable is [1, 3].
2. Morse potential, with minimum depth $D_e = 10$, located at $x_e = 2$. The exponent was chosen to be $\beta = 0.9$. The range of x is [1, 8].
3. Harmonic potential $^1/_2\ k(x - x_0)^2$, with $x_0 = 4$, $k = 0.002$. The range of x is [0, 8].
4. A realistic one-dimensional potential obtained from the $[Cl-H-Cl]^-$ system. The distance between chloride ions were fixed at 4.2 Å, and the position of the hydrogen atom was scanned along the chloride−chloride axis to obtain a total of 101 potential energy points at the B3LYP/6-31G level of theory.
5. A symmetric double-well potential $f_{DW}(x) = (x - 1)^2(x - 3)^2$ for $x \in [0.4, 3.6]$.
6. An asymmetric double-well $f_{ASD}(x) = (x - 2)^2[1 + 3(x - 5)^2]/10$ for $x \in [1, 6]$.
7. A damped double-well potential $f_{DDW}(x) = [(x - 1)^2(x - 3)^2 - 0.4]\exp(-1.5x)$. The range of x is [0.6, 8]. The well farther from the origin is relatively weak and may be interpreted as supporting a resonance state from dissociation.
8. A plane wave function $f_S(x) = \sin(x)$ for $x \in [0, {}^5/_2\ \pi]$.
9. A simple Gaussian function $f_G(x) = -6\ \exp[-(x - 4)^2]$ for $x \in [0, 8]$.
10. A real coherent state $f_{GM}(x) = \exp(-x^2/32)\cos(0.7x)$.

The last three functions are not standard potentials. These, however, have characteristics that a wave packet might possess.

For each of the above potentials the sampling function was calculated for a set of N_E values. In each case the values of I_V and $I_{V'}$ were scanned, and the normalized error was calculated according to

$$\sigma = \frac{\| f - f_{app} \|_2}{\| f - f_0 \|_2} \tag{29}$$

where $f_0 = (b - a)^{-1} \int_a^b f(x)\mathrm{d}x$, and $f_{app}(x)$ is the approximation to $f(x)$ obtained from sampling and interpolation. For all calculations $N_Q = 101$ and N_E were scanned in the range 6−51 which corresponds to compression factor α in the range 1/17 through 1/2. To cover even smaller values of α a second set of tests were carried out with $N_Q = 1001$ and the same values N_E as above. This resulted in compression ratios ranging from 1/170 through 1/20.

The behavior of the error is shown in Figure 2(a). In addition, deviations from the average error, due to the individual potentials, are indicated through the use of the

vertical bars in the figure. To understand these error values, consider the following interpretation of eq 29. The numerator of eq 29 is the L^2 norm of a difference vector when the potential is normalized as per the denominator. Using simple trigonometry one can see that the hyperangle between the *ket-vectors f* and f_{app} in a N_Q-dimensional linear vector space is approximately $\cos^{-1}[(2 - \sigma^2)/2]$ for small σ. Hence for $\sigma = 0.01$ (which is approximately the case for $N_E = 10$ in Figure 2(a)), the hyperangle between f and f_{app} is 0.57 degrees! Clearly, the error due to deterministic sampling and interpolation is negligible for $N_E > 15$ ($N_Q = 101$) and acceptable for $N_E = 11$. We will see in the next section that even smaller values of N_E can be used with acceptable error in vibrational spectroscopic properties, *and as the dimensionality of the problem increases, the method gets more efficient, exponentially*. This provides the opportunity for a large reduction in computational overhead within the current scheme.

To obtain a single set of values for I_V and $I_{V'}$ that work well on average, we first note that for complex systems the interaction potential is rarely a pure model potential such as those used here. In fact, these could in general possess a mixture of the complexities present in each individual function studied here. Consequently, for an optimal choice of I_V and $I_{V'}$ for realistic potentials we consider the average error

$$\sigma_{av}(I_V, I_{V'}) = \sum_i \frac{||f^i - f^i_{app}||_2}{||f^i - f^i_0||_2} \tag{30}$$

where the sum runs over all the model potentials. Figure 2(b) shows the normalized average potential error calculated according to eq 30 as a function of natural $\log(I_V + 1)$ and natural $\log(I_{V'} + 1)$ for $N_Q = 101$ and $N_E = 10$. The parameters, I_V and $I_{V'}$, are each scanned in the range 0−256. The minimum in the plot is at approximately $I_V = 1$ and $I_{V'} = 3$. Based on this analysis, we find that $I_V = 1$ and $I_{V'} = 3$ are suitable values that work well for the average case complexity, and, hence, these are the values chosen for the rest of the study in this publication.

To find an optimal I_χ we have conducted a series of one-dimensional wave packet dynamics simulations for the [Cl−H−Cl]$^-$ and [CH_3−H−Cl]$^-$ systems. Each simulation was 100 fs long, and there were a total of 70 simulations which helped us determine an optimal value for I_χ. For the case of the [Cl−H−Cl]$^-$, the shared proton is treated quantum dynamically, and two different sets of simulations have been conducted. In one case, the dynamics of the chloride ions and the electrons are treated using ADMP. In the other case, these are treated using Born−Oppenheimer dynamics. The choice of these systems was based on the following criteria. We needed to test the time-dependent deterministic sampling approach in conjunction with both ADMP and Born−Oppenheimer dynamics approximation. The [Cl−H−Cl]$^-$ system presents a simple test, since it is possible to constrain the Cl atoms at various distances and perform the dynamics; if the Born−Oppenheimer dynamics option were chosen for the chloride ions, the potential energy surface experienced by the wave packet would remain roughly the same. Hence this constitutes the simplest test case. However, if the ADMP dynamics option were chosen for the chloride ions, the potential energy surface would change as the wave packet moves, since the potential is determined in ADMP using the electronic density matrix at the wave packet centroid configuration. Hence the ADMP implementation presents a slightly more challenging test case. For the case of [CH_3−H−Cl]$^-$, again the shared proton is treated using quantum dynamics, while all other atoms are treated using ADMP. We constrain the carbon and chloride atoms to remain at a fixed distance; however, the three remaining hydrogen atoms are completely free to move according to the ADMP forces. Furthermore, since ADMP is used, the potential energy surface experienced by the wave packet changes with time. For all cases, a variety of basis sets was studied, and many values of N_E and I_χ were considered. Our results are summarized in Tables 1−3. In Table 1, the data obtained from Born−Oppenheimer subdynamics of the chloride ion (along with quantum wave packet dynamics of the shared proton) are summarized for two different basis sets, Cl−Cl distances, different N_E, and sampling parameter values. The σ_{N_E} values reported in these tables is described in eq 6, which again has the same physical interpretation as the error in eq 29. Hence, these errors are very small for many different values of I_χ. In Tables 2 and 3, the data obtained from ADMP subdynamics (along with quantum wave packet dynamics of the shared proton) are summarized for [Cl−H−Cl]$^-$ and [CH_3−H−Cl]$^-$, respectively. The reference wave packet for all cases is obtained from a full calculation (without sampling) over $N_Q = 101$ grid points. For all cases, the deterministic sampling parameters for potential and gradient

Table 1: Quantum Wave Packet Propagation Errors for the [Cl−H−Cl]$^-$ System[a]

I_V	$I_{V'}$	I_χ	σ_{21}	σ_{15}
		B3LYP/6-31G, $R = 4.2$ Å		
1	3	0	0.0000083	0.0001035
1	**3**	**1**	**0.0000036**	**0.0000720**
1	3	3	0.0000048	0.0000870
1	3	7	0.0000302	0.0003881
1	3	15	0.0003555	0.0069267
1	3	31	0.0079059	0.0491048
1	3	63	0.0331312	0.1068715
1	3	127	0.0581166	0.1515045
1	3	255	0.0732637	0.1826569
1	3	−1	0.0929057	0.2199152
		B3LYP/aug-cc-pVTZ, $R = 4.2$ Å		
1	3	0	0.0000171	0.0002318
1	**3**	**1**	**0.0000066**	**0.0001336**
1	3	−1	0.0066394	0.0492104
		B3LYP/aug-cc-pVTZ, $R = 3.6$ Å		
1	3	0	0.0000955	0.0013409
1	**3**	**1**	**0.0000405**	**0.0007540**
1	3	−1	0.2722858	0.4808945

[a] The shared proton is treated quantum-dynamically, while the chloride ions are treated using Born−Oppenheimer dynamics. Symbols σ_{21} and σ_{15} refer to wave packet errors as determined using eq 6 with $N_E = 21$ and $N_E = 15$, respectively. R represents the chloride−chloride distance. The optimal sampling parameters are shown in bold. $N_Q = 101$ is used for all cases.

Table 2: Quantum Wave Packet Propagation Errors for $[Cl-H-Cl]^-$ [a]

I_V	I_V'	I_χ	σ_{21}	σ_{15}
		B3LYP/6-31G, $R = 4.2$ Å		
1	3	−1	0.15531148	0.32244568
1	**3**	**1**	**0.00001817**	**0.00015913**
		B3LYP/aug-cc-pVTZ, $R = 3.6$ Å		
1	3	−1	0.17838404	0.53823434
1	3	0	0.00163375	0.21019838
1	**3**	**1**	**0.00020302**	**0.04537375**

[a] The shared proton is treated quantum-dynamically, while the rest of the system is treated using ADMP. Symbols σ_{21} and σ_{15} refer to wave packet errors as determined using eq 6 with $N_E = 21$ and $N_E = 15$, respectively. The optimal sampling parameters are shown in bold. $N_Q = 101$ is used for all cases.

Table 3: Quantum Wave Packet Propagation Errors for $[CH_3-H-Cl]^-$ [a]

I_V	I_V'	I_χ	σ_{21}	σ_{15}	σ_{11}
		B3LYP/6-311+G(d,p)			
1	3	−1	0.12067507	0.27055252	0.45599940
1	3	0	0.00003690	0.00083307	0.00783050
1	**3**	**1**	**0.00004855**	**0.00032730**	**0.00523513**

[a] The shared proton is treated quantum-dynamically, while the rest of the system is treated using ADMP. Symbols σ_{21}, σ_{15}, and σ_{11} refer to wave packet errors as determined using eq 6 with $N_E = 21$, $N_E = 15$, and $N_E = 11$, respectively. The optimal sampling parameters are shown in bold. $N_Q = 101$ in all cases.

have been set to the previously found optimal values of $I_V = 1$ and $I_{V'} = 3$.

We find that $I_\chi = 1$ is the optimal value for quantum wave packet simulation with $I_V = 1$ and $I_{V'} = 3$. The corresponding entries in Tables 1−3 are shown in bold. To further substantiate the accuracy of the sampling approach, in Figure 3 we present the time-evolution of the L^2-norm of the error in the potential (extrapolated potential based on deterministic sampling minus the reference potential calculated on all grid points) for long simulations (10 ps). As can be seen the error is minimal and well within the acceptable range for DFT electronic structure calculations. Furthermore, $N_E = 11$ represents a sizable reduction in the number of grid points where potential evaluations need to be conducted. We further note that the results for the B3LYP/6-31G, $R = 4.2$ Å calculations on the $[Cl-H-Cl]^-$ system described in Table 1 are rather important. *First, at this geometry, the zero-point energy of the proton (≈2 milli-Hartrees) is comparable to the height of the barrier (≈4 milli-Hartrees) separating the protonated states on each chloride. Furthermore, there are multiple states accessible below the barrier and immediately above the barrier. This provides the opportunity for tunneling, zero point effects, and overbarrier reflection of the wave packet playing an important role in the dynamics.* It is interesting to note that the time-dependent sampling measure performs well even under these highly quantum-mechanical, tunneling oriented conditions.

To analyze the physics behind the choice, $I_\chi = 1$, $I_V = 1$, and $I_{V'} = 3$, using eq 11, let us consider two separate regions of a potential energy surface that are of interest in quantum dynamics. (a) Minimum energy region of the potential surface: The region where the potential energy is low, the wave packet amplitude may be high, and the gradient here is generally small. (b) The region where the potential is high and the gradient is also high represents the region of a potential surface that could mark the advent of tunneling. This region also generally comprises a classical turning point, and the standard semiclassical approximation breaks down[80] in this region. (Also see Appendix A.) Thus, this is an interesting region in quantum dynamical simulations, and, on average, the wave packet amplitude may be expected to be small in such regions. In eq 11 the quantities $\tilde{\rho}$, $\tilde{E}'$, and $\tilde{E}$ are each in the region [0,1] (see discussion before eq 11) and hence for region (a)

$$[\omega_0^{1,3,1}]_{\text{Case(a)}} = constant * \frac{[1 + 1/1] \times [0 + 1/3]}{0 + 1/1} = constant * 2/3 \quad (31)$$

where we have used $I_\chi = 1$, $I_V = 1$, and $I_{V'} = 3$ in eq 11 and also substituted the maximum values of $\tilde{\rho}$ and minimum possible values of $\tilde{E}'$ and $\tilde{E}$ as required by the definition of region (a) above. Now, in region (b), the tunneling and classical turning-point regions

$$[\omega_0^{1,3,1}]_{\text{Case(b)}} = constant * \frac{[0 + 1/1] \times [1 + 1/3]}{1 + 1/1} = constant * 2/3 \quad (32)$$

That is, the choice of $I_\chi = 1$, $I_V = 1$, and $I_V' = 3$ provides an equal distribution of grid points in low potential regions as well as tunneling regions.

There can be other possible values of I_χ, I_V, and I_V' that also have the property of producing an equal distribution of grid points in regions (a) and (b). For the special case of $I_\chi = I_V$ it is possible to show that

$$I_V' = (I_\chi + 1)^2 - 1 \quad (33)$$

will always provide an equal distribution of points in regions (a) and (b). (We have only considered $I_\chi = I_V$ in this analysis since one would expect the potential and the wave packet amplitude to behave in a mutually complementary fashion.) However, for larger values of I_χ, I_V, and I_V' (larger than 1,3,1) the distribution of points in other classically forbidden regions (regions of high potential and low gradient) becomes smaller, and hence the choice $I_\chi = 1$, $I_V = 1$, and $I_V' = 3$ provides a good physical choice as is seen from the numerical experiments described in this section.

B. Quantum Dynamical Treatment of Hydrogen Transfer in Soybean Lipoxygenase-1 (SLO-1) and Treatment of the Shared Proton in $[Cl-H-Cl]^-$. To study the scaling of errors with dimensionality and system complexity, we have considered (a) the $[Cl-H-Cl]^-$ system again but with full three-dimensional quantum wave packet treatment of the shared proton and (b) soybean lipoxygenase-1 (SLO-1) which has been thought to exhibit hydrogen tunneling in recent literature.[119−125] SLO-1 is a non-heme metalloenzyme that catalyzes the oxidation of unsaturated fatty acids. The active site for the enzyme is shown in Figure 4(a) and the model for the active site used in our study is shown in Figure 4(b). The rate-determining step in the catalytic cycle for SLO-1 involves the abstraction of a hydrogen atom from the fatty acid chain by the octahedral $Fe^{3+}-OH$ complex present in the active site and shows a remarkably large H/D kinetic isotope effect of 81 near room temperature and a weak

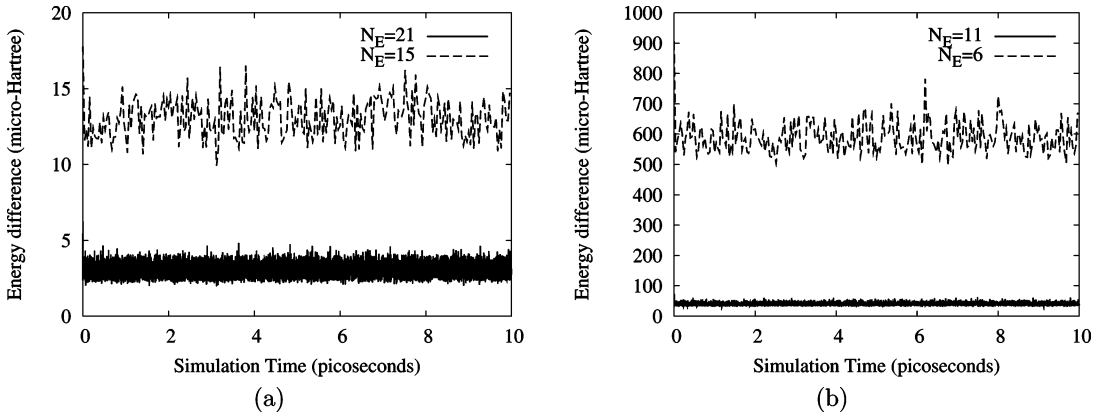

Figure 3. The error in the interpolated potential energy, for the $[Cl-H-Cl]^-$ system, from using time-dependent deterministic sampling during the wave packet dynamics calculations. The shared hydrogen is treated as a one-dimensional quantum wave packet discretized over $N_Q = 101$ regularly spaced grid points. As can be seen the errors in the potential energy for N_E greater than 11 are in the microhartree range.

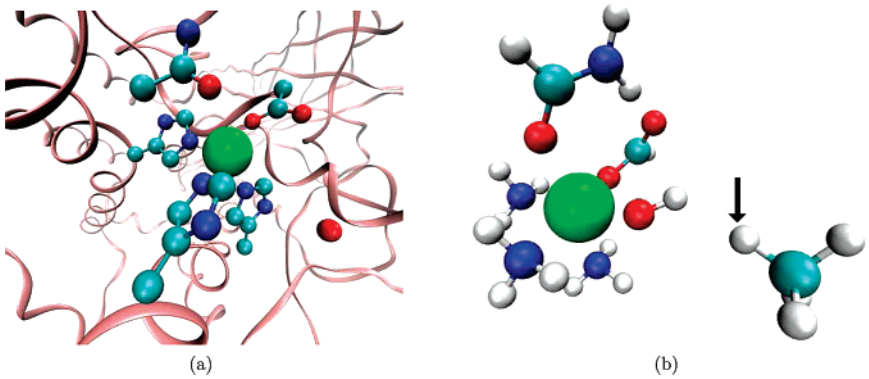

Figure 4. Soybean lipoxygenase-1: The active site is shown in part (a), and the model used for the active site in the current study, after geometry optimization, is shown in part (b). The iron atom is represented by the large sphere close to the center of the two figures. The shared hydrogen atom is marked. Note that in our study the three imidazole rings have been terminated with amine groups.

temperature dependence of the reaction rate constant.[120] These observations are thought to reflect the fact that hydrogen transfer occurs extensively via a tunneling mechanism.[120−123]

In this section we consider SLO-1 to study the scaling of errors in the methodology with respect to dimensionality and system complexity and to demonstrate the power of our methodology in attacking large complex problems. We simplify the active site by substituting amine groups for the imidazole rings. Since the purpose of the current section is only to illustrate the scaling of errors in the deterministic sampling methodology, a detailed study of the SLO-1 problem, using wave packet ab initio molecular dynamics along with a more elaborate description of the active site and substrate, to evaluate the extent of nuclear quantum effects will be the subject of a future publication.

To study the evolution of errors, we considered frozen geometries for both $[Cl-H-Cl]^-$ and SLO-1 where a potential energy scan was performed along a three-dimensional Cartesian grid for the shared hydrogen atom. In addition to the electronic energy (at the level of B3LYP/6-31+G**) we also computed gradients of the electronic energy at each grid point for use with the sampling algorithm. (Note: this does not constitute additional effort since the gradients are required to be computed to propagate the classical nuclear degrees of freedom and the electrons for the case of a full wave packet ab initio dynamics calculation.) Once the potential energy surface was obtained, the eigenstates for the quantum nuclei were obtained using the Arnoldi iterative diagonalization procedure.[101,126,127] The Arnoldi scheme is a variant of the Lanczos procedure[101] and involves the repetitive application of the Hamiltonian matrix to an initial vector to form a Krylov basis set.[101] The representation of the Hamiltonian in this new basis set leads to a Hessenberg form or tridiagonal form[101] for the Hamiltonian, which is relatively easy to diagonalize. The action of the Hamiltonian matrix on any vector is calculated easily by taking advantage of the sparse structure of the DAF kinetic energy operator (second derivative of the zero Δt_{QM} limit of eq 5) and the fact that the full three-dimensional kinetic energy operator can be written in direct product form which obviates the need to store the full (million by million) Hamiltonian matrix. For a grid comprising 101 points in each direction (that is, a million points in three dimensions) we only store three 101×101 sparse matrices that are used to construct the action of the full Hamiltonian matrix on a vector as required by the Arnoldi scheme. This is also the case for propagation of a wave packet in three dimensions, where again we only

Table 4: Quantum Wave Packet Propagation Errors for [Cl−H−Cl]$^-$ and Soybean Lipoxygenase-1 (SLO-1)[d]

[Cl−H−Cl]$^-$	$\sigma_{101}{}^3$	$\sigma_{11}{}^3$	$\sigma_{15}{}^3$	$\sigma_{21}{}^3$
20th[a]	3.059×10^{-08}	6.660×10^{-04}	1.989×10^{-04}	5.221×10^{-05}
seventh[a]	2.219×10^{-08}	3.999×10^{-03}	5.275×10^{-05}	1.176×10^{-04}
first[a]	1.079×10^{-08}	2.614×10^{-02}	1.308×10^{-03}	3.429×10^{-04}
thermal sampling[b]	1.066×10^{-08}	3.433×10^{-02}	1.491×10^{-04}	2.785×10^{-04}
Gaussian[c]	7.243×10^{-07}	6.037×10^{-03}	1.182×10^{-04}	8.640×10^{-05}
SLO-1	$\sigma_{101}{}^3$	$\sigma_{11}{}^3$	$\sigma_{15}{}^3$	$\sigma_{21}{}^3$
20th[a]	2.812×10^{-03}	7.324×10^{-01}	1.913×10^{-01}	4.421×10^{-01}
first[a]	3.140×10^{-05}	4.500×10^{-01}	8.927×10^{-01}	2.027×10^{-01}
thermal sampling[b]	4.541×10^{-05}	5.558×10^{-01}	7.492×10^{-01}	1.371×10^{-01}
Gaussian[c]	1.593×10^{-03}	6.998×10^{-03}	4.593×10^{-03}	2.356×10^{-03}

[a] Number represents the eigenstates number that is used as initial wave packet. [b] Initial wave packet is constructed as a linear combination of eigenstate with coefficients for the ith eigenstate: $\exp[-E_i/kT]$. Temperature = 300 K. [c] Initial wave packet is a Gaussian centered close to the top of the barrier. [d] Symbols $\sigma_{21}{}^3$, $\sigma_{15}{}^3$, and $\sigma_{11}{}^3$ refer to wave packet errors as determined using eq 6 with $N_E = 21^3$, $N_E = 15^3$, and $N_E = 11^3$, respectively. $N_Q = 101^3$ in all cases. Total time of propagation for all cases is 500 fs.

store three one-dimensional free propagators, eq 5, to construct the evolution of a three-dimensional wave packet.

The eigenvectors obtained from the Arnoldi process are then used to construct initial wave packets, as described in Table 4, and propagated with and without deterministic sampling, and the propagation errors are compared in Table 4. Here, the wave packet is propagated at each step, and the potential, gradient, and wave packet at N_E grid points are used to compute a sampling function for the next step. This sampling function is then used to obtain a new grid distribution of N_E points (potentially different from the N_E points used in the previous step) which are then used for to propagate the wave packet. The errors in Table 4 indicate that reasonable accuracy in the propagation is obtained using only 11 grid points per dimension.

C. Comparison of Vibrational Properties for Different Values of N_E. As a further test and illustrative calculation, we present the quantum dynamically averaged vibrational density of states from wave packet ab initio dynamics simulations. It is well-known that the Fourier transform of the velocity−velocity autocorrelation represents the vibrational density of states and has been widely used in classical dynamics[128,129] as well as in ab initio molecular dynamics.[95,130] Quantum corrections to such classical correlation functions[131−133] are an important problem in chemical physics.

In our case, the existence of classical and quantum-dynamical nuclei complicates the direct application of the velocity correlation concept. To provide a cogent treatment we exploit the fact that the quantum correspondence to the classical nuclear velocity is given in terms of the probability flux (or probability current)[80]

$$\mathcal{J}(x,t) = \frac{\hbar}{2m\imath}[\psi^*(x,t)\nabla\psi(x,t) - \psi(x,t)\nabla\psi^*(x,t)]$$
$$= \frac{\hbar}{m}\mathcal{I}[\psi^*(x,t)\nabla\psi(x,t)] \quad (34)$$

where $\mathcal{I}[A]$ represents the imaginary portion of the complex number A. Thus to construct the velocity−velocity autocorrelation function, we consider the average flux (or the expectation value of flux) at any given time

$$\mathbf{J}(t) = \langle \mathcal{J} \rangle = \mathcal{R}\left[\left\langle \psi(t)\middle|\frac{-\imath\hbar}{m}\nabla\middle|\psi(t)\right\rangle\right] \quad (35)$$

to be used in conjunction with the classical nuclear velocities. The symbol $\mathcal{R}$ represents the real part of the bracketed quantity.

We thus, simultaneously, construct the correlation functions $\langle \mathbf{J}(t)\mathbf{J}(0)\rangle$ and $\langle v(t)v(0)\rangle$ and the full vibrational density of states as the cumulative Fourier transform

$$C(\omega) = \int_{-\infty}^{+\infty} \exp[-\imath\omega t]\{\langle v(t)v(0)\rangle_C + \langle \mathbf{J}(t)\mathbf{J}(0)\rangle_Q\} \quad (36)$$

where the symbols $\langle\cdots\rangle_C$ and $\langle\cdots\rangle_Q$ represent the classical and quantum variables ensemble averages.

In Figure 5 we present the vibrational density of states for [Cl−H−Cl]$^-$ from full three-dimensional treatment of the shared hydrogen atom. The results for the uninterpolated study are shown in Figure 5(a), and these are comparable to the experimental results in ref 134. The observed ν_3 band is approximately at 722 cm^{-1}, while the strongest peak in Figure 5(a) is close to 750 cm^{-1}. The discrepancy is explained based on the fact that the Cl−Cl distance used in our simulations are different from those seen in the experiment.[134] In Figure 5(b) we provide the difference spectrum of errors for $N_E = (11)^3$, $(15)^3$, and $(21)^3$ with $N_Q = (101)^3$. It is interesting to note that $N_E = (11)^3$ reproduces the spectrum well in comparison with the full $N_Q = (101)^3$ calculation resulting in a *truly extraordinary compression of the quantum grid and a computational gain of approximately 3 orders of magnitude*. All three-dimensional calculations here used the marginal sampling approach discussed in section IV B.

VI. Concluding Remarks

In this paper, we present a computational scheme to improve the efficiency of our recently developed approach to perform simultaneous dynamics of electrons and nuclei[59] through quantum wave packet ab initio dynamics. A robust and efficient potential adapted time-dependent, deterministic, sampling scheme is derived which improves the efficiency associated with the calculation of the interaction potential between the ab initio system and quantum wave packet. This interaction potential can now be dynamically constructed on a sparse, irregular grid based on deterministic sampling that takes into account the potential energy function at the previous dynamics step, its gradients, and instantaneous density of the wave packet. The sampling criterion has the

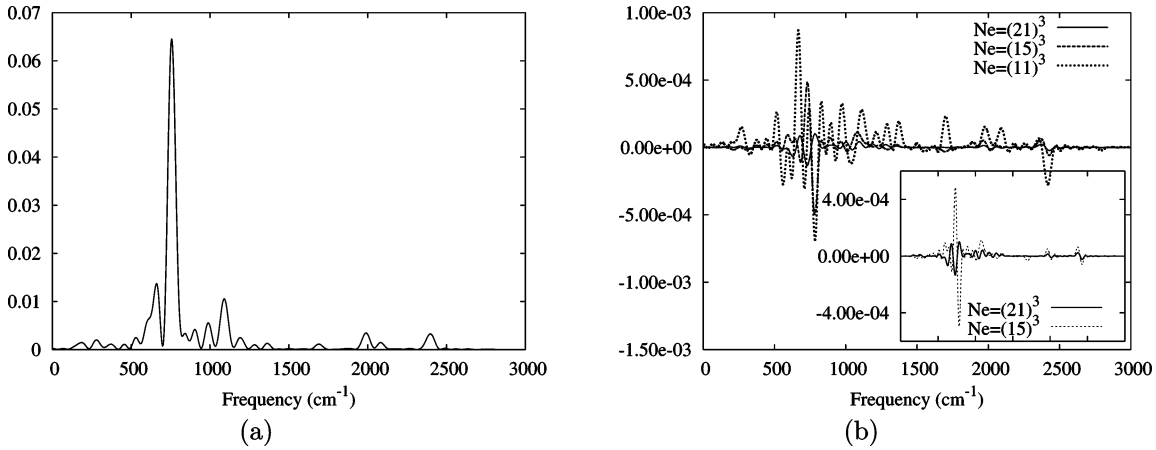

Figure 5. The [Cl−H−Cl]⁻ vibrational states obtained using eq 36 with the shared hydrogen treated as a three-dimensional wave packet. Part (a) represents the spectrum without time-dependent deterministic sampling for $N_Q = 101$.[3] Part (b) describes the difference spectrum for different values of N_E. All spectra are obtained from 500 fs dynamics data.

attractive feature that it targets regions of the potential that are rapidly varying or lower in energy. In addition, it uses the wave packet density at the previous step to attenuate the distribution of grid points. We have also constructed a cumulative correlation function that includes velocity correlation for the classical degrees of freedom and flux correlation for the quantum dynamical degrees of freedom to obtain the vibrational density of states, inclusive of quantum dynamical effects. The vibrational density of states is used as a tool to check the accuracy of the dynamic sampling algorithm, but the methodology seems general and has promise within the current dynamical framework.

The dynamic sampling function has three adjustable parameters that have been optimized to present an accurate and efficient "on-the-fly" fit of the time-dependent potential. We find that using the sampling function *accurate dynamical and spectral properties can be obtained from only a small fraction of the grid points.* For cases when a single particle is treated quantum mechanically in a bath of surrounding electrons and classical nuclei, the regular grid describing the quantum wave packet can be compressed by several orders of magnitude using the dynamical sampling algorithm and still retain accuracy at a high level. Since the compressed grid is where the electronic energies are determined during the dynamics, this represents an enormous reduction in computational cost. The computational methodology has been demonstrated for both ADMP and Born−Oppenheimer treatment of the classical nuclear and electronic degrees of freedom in conjunction with wave packet propagation.

Acknowledgment. We acknowledge the support of the Camille and Henry Dreyfus New Faculty awards program, the Arnold and Mabel Beckman Young Investigator Award Program, and the Indiana University, Chemistry Department.

Appendix A: A Few Comments on the Physical Interpretation of Eq 7: Connections to WKB Semiclassical Theory and Bohmian Mechanics

Another physical interpretation for the function in eq 7 can be obtained by recognizing its connection to the Wentzel−Kramers−Brillouin (WKB)[80] semiclassical theory. To expound further on this aspect we first introduce the fact that the semiclassical approximation is accurate when

$$\frac{p}{\hbar} \equiv \lambda^{-1} \gg \left(\frac{1}{E - V(x)}\right)\frac{\partial V}{\partial x} \qquad \text{(A1)}$$

i.e. the slowly varying limit of the potential compared to the momentum of the particle and inverse de Broglie wavelength. The sampling function in eq 7 has the property that it is directly proportional to $\partial V/\partial x$ and inversely proportional to the potential. [The modification to the sampling scheme discussed in eq 8 retains this functional dependence.] Hence, $\omega_0(R_{QM})$ is inversely proportional to the WKB length scale λ (or local de Broglie wavelength) in the sense that a greater number of potential evaluations are directed to regions where the potential is rapidly varying and the WKB length scale is smaller. This has the following implications: when the right side of eq A1 is too large, a semiclassical approximation has a greater propensity to failure (unless the momentum of the particle is suitably large). However, for the current methodology, when the right-hand side of eq A1 is large, i.e. when the potential is rapidly varying or when the potential is low, then the sampling function has a larger magnitude which leads to additional potential evaluations in this region. Hence the current approach makes a greater effort to perform accurate quantum dynamics in regions of a potential where a semiclassical approximation may break down. (Also see the discussion at the end of section V A.)

A second important connection may be obtained by understanding the behavior of ω_0 in the vicinity of a wave packet nodal region. This is precisely the region where novel implementations of quantum dynamics based on Bohm's interpretation[80−87,104−108] have trouble on account of the fact that the "quantum potential" $[= (-\hbar^2/2m)\rho^{-1/2}\nabla^2\rho^{1/2}]$ in Bohmian dynamics becomes singular in the vicinity of a node. In our case, the distribution of potential evaluation points is determined not only by the wave packet amplitude but also the potential and its gradients. Hence, if the potential energy is low in the vicinity of a node (as would be the case for nodes enforced by symmetry) or the gradient is high,

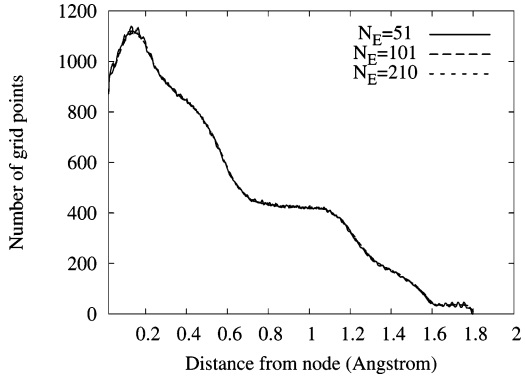

Figure 6. The figure represents the distribution of potential evaluation points obtained from eq 7 in the vicinity of a node. (N_Q = 901.) The maximum at 0.15 Å and the substantial probability close to zero indicates that the current formalism maintains an acceptable level of sampling close to nodal points.

then that region is well represented by the current algorithm. Figure 6 shows the number of grid points where potential evaluations are performed as a function of distance from the nearest node. The sampling function in eq 7, along with the algorithm discussed in section IV A 1, is used to determine the location of the N_E grid points. As seen in Figure 6, there exists a substantial probability of finding grid points close to a node when the sampling measure introduced here is used. This was the case over a wide range of N_E. The ADMP potential used for this calculation is a double well potential. The number of nodes is determined dynamically, and the spontaneous appearance or disappearance of nodes is allowed, since the quantum dynamics methodology used here permits wave packet splitting.

Appendix B: Time-Dependent Hermite Curve Interpolation of the Potential Energy Surface

The interpolation scheme used here makes full utilization of the availability of potential and gradients and is described in this section. The scheme discussed here is a special case of cubic spline interpolation[135] and is known as Hermite curve interpolation.[116,117] Consider a function, $f(x)$, defined in an interval $[x_0, x_1]$ with the value of the function and the first derivative at the end points given as $\{f_{x_0}, f_{x_1}, f'_{x_0}, f'_{x_1}\}$. The function can then be approximated using a third-order polynomial in $[x_0, x_1]$ as

$$f(x) \approx f_{app}(x) = f_{x_0}\nu_{x_0}(x) + f_{x_1}\nu_{x_1}(x) + f'_{x_0}\nu'_{x_0}(x) + f'_{x_1}\nu'_{x_1}(x) \tag{B1}$$

where the weights are defined as

$$\nu_{x0}(x) = 2\tilde{x}^3 - 3\tilde{x}^2 + 1 \tag{B2}$$

$$\nu_{x_1}(x) = -2\tilde{x}^3 + 3\tilde{x}^2 \tag{B3}$$

$$\nu'_{x_0}(x) = (\tilde{x}^3 - 2\tilde{x}^2 + \tilde{x})(x_1 - x_0) \tag{B4}$$

$$\nu'_{x_1}(x) = (\tilde{x}^3 - \tilde{x}^2)(x_1 - x_0) \tag{B5}$$

$$\tilde{x} = \frac{x - x_0}{x_1 - x_0} \tag{B6}$$

For our purposes the values f_{x_k} and f'_{x_k} represent the potential energy and the derivative of potential energy with respect to the quantum grid on N_E grid points. The multidimensional generalization is conducted in a similar fashion using the potential and gradient values available at every grid point.

Appendix C: Convergence of the Spreading Transformation

The aim of the spreading transformation is to disperse the excess density $||\Omega_i\tilde{\omega}_i||_1$, as described in section IV A1. This is done through the iterative scheme in eq 27, and it is necessary to evaluate the convergence properties of this scheme. Toward this we define the positive semidefinite convergence measure

$$g_i \equiv ||\Omega_i\tilde{\omega}_i||_1 \geq 0 \tag{C1}$$

When g_i is greater than a numerical threshold, the spreading transformation is not converged at the ith iteration, and the excess density (g_i) needs to be spread onto the region determined by Ω_i^c. As a consequence of eq 14 and the normalization condition in eq 12, it follows that $\Omega_i^c \neq 0$ when $g_i > 0$. Furthermore, since Ω_i^c is a projection operator, $||\{\Omega_i^c\mathbf{1}\}||_1 > 0$. The spreading transformation then leads to new values for ω_{i+1} as per eq 27, Ω_{i+1} and g_{i+1} given by

$$g_{i+1} = ||\Omega_{i+1}\tilde{\omega}_{i+1}||_1 \tag{C2}$$

Using eq 27 we obtain

$$\begin{aligned} g_{i+1} &= \int_a^b \Omega_{i+1}(\omega_{i+1} - \alpha^*)\mathrm{d}x \\ &= \int_a^b \Omega_{i+1}\left\{\Omega_i\alpha^* + \Omega_i^c\left(\frac{||\Omega_i\tilde{\omega}_i||_1}{||\{\Omega_i^c\mathbf{1}\}||_1} + \omega_i\right) - \alpha^*\right\}\mathrm{d}x \\ &= \int_a^b \Omega_{i+1}\Omega_i^c\left\{-\alpha^* + \frac{||\Omega_i\tilde{\omega}_i||_1}{||\{\Omega_i^c\mathbf{1}\}||_1} + \omega_i\right\}\mathrm{d}x \end{aligned} \tag{C3}$$

The operators Ω_{i+1} and Ω_i^c are both projection operators, and Ω_{i+1} is created from spreading g_i onto Ω_i^c. Thus,

$$\Omega_{i+1}\Omega_i^c = (\Omega_{i+1} - \Omega_i) = (\Omega_i^c - \Omega_{i+1}^c) \equiv L_i \tag{C4}$$

Using this in eq C3, we obtain

$$\begin{aligned} g_{i+1} &= \int_a^b (\Omega_{i+1} - \Omega_i)\tilde{\omega}_i dx + g_i\frac{||\{\Omega_i^c\mathbf{1}\}||_1 - ||\{\Omega_{i+1}^c\mathbf{1}\}||_1}{||\{\Omega_i^c\mathbf{1}\}||_1} \\ &= \int_a^b L_i\tilde{\omega}_i dx + g_i\left(1 - \frac{||\{\Omega_{i+1}^c\mathbf{1}\}||_1}{||\{\Omega_i^c\mathbf{1}\}||_1}\right) \end{aligned} \tag{C5}$$

However, since the subspace represented by $(\Omega_{i+1} - \Omega_i) \equiv L_i$ is orthogonal to the subspace represented by Ω_i, this implies $\forall_{x\in L_i}$: $\omega_i(x) < \alpha^*$, and hence $\int_a^b L_i\tilde{\omega}_i dx \leq 0$ where

the equality holds only when $\Omega_i = 0$. Hence,

$$g_{i+1} \leq g_i\left(1 - \frac{||\{\Omega_{i+1}^c \mathbf{1}\}||_1}{||\{\Omega_i^c \mathbf{1}\}||_1}\right) \tag{C6}$$

But, by definition $g_{i+1} > 0$, and hence

$$0 \leq g_{i+1} \leq g_i\left(1 - \frac{||\{\Omega_{i+1}^c \mathbf{1}\}||_1}{||\{\Omega_i^c \mathbf{1}\}||_1}\right) \tag{C7}$$

or

$$0 \leq \frac{g_{i+1}}{g_i} \leq \left(1 - \frac{||\{\Omega_{i+1}^c \mathbf{1}\}||_1}{||\{\Omega_i^c \mathbf{1}\}||_1}\right) \tag{C8}$$

Now we consider three different limiting cases for the quantity $||\{\Omega_{i+1}^c \mathbf{1}\}||_1/||\{\Omega_i^c \mathbf{1}\}||_1$ in eq C8 and study the convergence properties of the sequence $\{g_i\}$ for all these cases. It is first important to note that

$$0 \leq \frac{||\{\Omega_{i+1}^c \mathbf{1}\}||_1}{||\{\Omega_i^c \mathbf{1}\}||_1} \leq 1 \tag{C9}$$

Since Ω_{i+1}^c is created after spreading in the *i*th iteration, the range of the subspace Ω_{i+1}^c is smaller than that of Ω_i^c. Hence,

1. $||\{\Omega_{i+1}^c \mathbf{1}\}||_1/||\{\Omega_i^c \mathbf{1}\}||_1 = 1$. It then follows that $0 \leq g_{i+1} \leq 0g_i$, which means that $g_{i+1} = 0$, that is spreading transformation has converged at the $(i + 1)$th iteration.

2. $||\{\Omega_{i+1}^c \mathbf{1}\}||_1/||\{\Omega_i^c \mathbf{1}\}||_1 = 0$. In this case $||\Omega_{i+1}^c||_1 = 0$. If g_{i+1} is nonzero this implies that there exists an excess density but *no region to "spread" the excess density*. This is in violation of the normalization condition eq 12 and thus $g_{i+1} = 0$ if $||\Omega_{i+1}^c||_1 = 0$ which again implies that the spreading transformation has converged at the $(i + 1)$th iteration.

3. $0 < ||\{\Omega_{i+1}^c \mathbf{1}\}||_1/||\{\Omega_i^c \mathbf{1}\}||_1 < 1$ which leads to $[0 < g_{i+1}/g_i < (1 - ||\{\Omega_{i+1}^c \mathbf{1}\}||_1/||\{\Omega_i^c \mathbf{1}\}||_1)]$, where the upper bound is less that 1. According to de Alembert's ratio test[136] the series comprising $\{g_i\}$ converges when this ratio is less than 1. Hence, by extension the $\{g_i\}$ must converge, is a monotonic decreasing sequence, and is lower bounded by zero.

References

(1) *Dynamics of Molecules and Chemical Reactions;* Wyatt, R. E., Zhang, J. Z. H., Eds.; Marcel Dekker Inc.: New York, New York, 1996.

(2) *Classical and quantum dynamics in condensed phase simulations;* Berne, B. J., Ciccotti, G., Coker, D. F., Eds.; World Scientific: 1997.

(3) Schatz, G. C.; Kupperman, A. *J. Chem. Phys.* **1976**, *65*, 4642.

(4) Delos, J. B. *Rev. Mod. Phys.* **1981**, *53*, 287.

(5) Feit, M. D.; Fleck, J. A. *J. Chem. Phys.* **1982**, *78*, 301.

(6) Kosloff, R. *Annu. Rev. Phys. Chem.* **1994**, *45*, 145.

(7) Leforestier, C.; Bisseling, R. H.; Cerjan, C.; Feit, M. D.; Freisner, R.; Guldberg, A.; Hammerich, A.; Jolicard, D.; Karrlein, W.; Meyer, H. D.; Lipkin, N.; Roncero, O.; Kosloff, R. *J. Comput. Phys.* **1991**, *94*, 59.

(8) DeVries, P. In *Atomic and molecular processes with short intense laser pulses*; Bandrauk, A. D., Ed.; Plenum Press: New York, 1988; Vol. 171 of *NATO ASI Series B.; Physics*, p 481.

(9) Jang, H. W.; Light, J. C. *J. Chem. Phys.* **1995**, *102*, 3262−3268.

(10) Althorpe, S. C.; Clary, D. C. *Annu. Rev. Phys. Chem.* **2003**, *54*, 493−529.

(11) Althorpe, S. C.; Fernandez-Alonso, F.; Bean, B. D.; Ayers, J. D.; Pomerantz, A. E.; Zare, R. N.; Wrede, E. *Nature* **2002**, *416*, 67−70.

(12) Huang, Y.; Iyengar, S. S.; Kouri, D. J.; Hoffman, D. K. *J. Chem. Phys.* **1996**, *105*, 927.

(13) Miller, W. H.; Schwartz, S. D.; Tromp, J. W. *J. Chem. Phys.* **1983**, *79*, 4889.

(14) Makri, N. *Comput. Phys. Comm.* **1991**, *63*, 389−414.

(15) Cao, J.; Voth, G. A. *J. Chem. Phys.* **1994**, *100*, 5106.

(16) Jang, S.; Voth, G. A. *J. Chem. Phys.* **1999**, *111*, 2357.

(17) Feit, M. D.; Fleck, J. A. *J. Chem. Phys.* **1983**, *79*, 301.

(18) Feit, M. D.; Fleck, J. A. *J. Chem. Phys.* **1984**, *80*, 2578.

(19) Kosloff, D.; Kosloff, R. *J. Comput. Phys.* **1983**, *52*, 35.

(20) Kosloff, D.; Kosloff, R. *J. Chem. Phys.* **1983**, *79*, 1823.

(21) Tal-Ezer, H.; Kosloff, R. *J. Chem. Phys.* **1984**, *81*, 3967.

(22) Hartke, B.; Kosloff, R.; Ruhman, S. *Chem. Phys. Lett.* **1986**, *158*, 223.

(23) Iyengar, S. S.; Kouri, D. J.; Hoffman, D. K. *Theor. Chem. Acc.* **2000**, *104*, 471.

(24) Lill, J. V.; Parker, G. A.; Light, J. C. *Chem. Phys. Lett.* **1982**, *89*, 483.

(25) Light, J. C.; Hamilton, I. P.; Lill, J. V. *J. Chem. Phys.* **1985**, *82*, 1400.

(26) Colbert, D. T.; Miller, W. H. *J. Chem. Phys.* **1992**, *96*, 1982−1991.

(27) Huang, Y.; Kouri, D. J.; Arnold, M.; Thomas L. Marchioro, I.; Hoffman, D. K. *Comput. Phys. Comm.* **1994**, *80*, 1.

(28) Wang, I. S. Y.; Karplus, M. *J. Am. Chem. Soc.* **1973**, *95*, 8160.

(29) Leforestier, C. *J. Chem. Phys.* **1978**, *68*, 4406.

(30) Car, R.; Parrinello, M. *Phys. Rev. Lett.* **1985**, *55*, 2471.

(31) Bolton, K.; Hase, W. L.; Peslherbe, G. H. World Scientific: Singapore, 1998; Chapter: Direct Dynamics of Reactive Systems, p 143.

(32) Schlegel, H. B.; Millam, J. M.; Iyengar, S. S.; Voth, G. A.; Daniels, A. D.; Scuseria, G. E.; Frisch, M. J. *J. Chem. Phys.* **2001**, *114*, 9758.

(33) Deumens, E.; Diz, A.; Longo, R.; Öhrn, Y. *Rev. Mod. Phys.* **1994**, *66*, 917.

(34) Hack, M. D.; Truhlar, D. G. *J. Phys. Chem. A* **2000**, *104*, 7917−7926.

(35) Jasper, A. W.; Zhu, C.; Nangia, S.; Truhlar, D. G. *Faraday Discuss.* **2004**, *127*, 1−22.

(36) Miller, W. H. *J. Phys. Chem. A* **2001**, *105*, 2942−2955.

(37) Heller, E. J. *J. Chem. Phys.* **1975**, *62*, 1544−1555.

(38) Fiete, G. A.; Heller, E. J. *Phys. Rev. A* **2003**, *68*, 022112.

(39) Hammes-Schiffer, S.; Tully, J. *J. Chem. Phys.* **1994**, *101*, 4657−4667.

(40) Ben-Nun, M.; Quenneville, J.; Martinez, T. J. *J. Phys. Chem. A* **2000**, *104*, 5161.

(41) Coe, J. D.; Martinez, T. J. *J. Am. Chem. Soc.* **2005**, *127*, 4560.

(42) Martinez, T. J.; Ben-Nun, M.; Ashkenazi, G. *J. Chem. Phys.* **1996**, *104*, 2847.

(43) Martinez, T. J.; Levine, R. D. *J. Chem. Phys.* **1996**, *105*, 6334.

(44) Micha, D. A. *J. Phys. Chem. A* **1999**, *103*, 7562−7574.

(45) Gerber, R. B.; Buch, V.; Ratner, M. A. *J. Chem. Phys.* **1982**, *77*, 3022.

(46) Bisseling, R. H.; Kosloff, R.; Gerber, R. B.; Ratner, M. A.; Gibson, L.; Cerjan, C. *J. Chem. Phys.* **1987**, *87*, 2760−2765.

(47) Makri, N.; Miller, W. H. *J. Chem. Phys.* **1987**, *87*, 5781−5787.

(48) McCoy, A.; Gerber, R. B.; Ratner, M. A. *J. Chem. Phys* **1994**, *101*, 1975.

(49) Payne, M. C.; Teter, M. P.; Allan, D. C.; Arias, T. A.; Joannopoulos, J. D. *Rev. Mod. Phys.* **1992**, *64*, 1045.

(50) Marx, D.; Hutter, J. John von Neumann Institute for Computing: Julich, 2000; Vol. 1, Chapter: Ab Initio Molecular Dynamics: Theory and Implementation, pp 301−449.

(51) Schlegel, H. B. *J. Comput. Chem.* **2003**, *24*, 1514−1527.

(52) Andersen, H. C. *J. Chem. Phys.* **1980**, *72*, 2384−2393.

(53) Parrinello, M.; Rahman, A. *Phys. Rev. Lett.* **1980**, *45*, 1196−1199.

(54) Remler, D. K.; Madden, P. A. *Mol. Phys* **1990**, *70*, 921.

(55) Iyengar, S. S.; Schlegel, H. B.; Millam, J. M.; Voth, G. A.; Scuseria, G. E.; Frisch, M. J. *J. Chem. Phys.* **2001**, *115*, 10291.

(56) Pavese, M.; Berard, D. R.; Voth, G. A. *Chem. Phys. Lett.* **1999**, *300*, 93−98.

(57) Tuckerman, M. E.; Marx, D. *Phys. Rev. Lett.* **2001**, *86*, 4946−4949.

(58) Chen, B.; Ivanov, I.; Klein, M. L.; Parrinello, M. *Phys. Rev. Lett.* **2003**, *91*, 215503.

(59) Iyengar, S. S.; Jakowski, J. *J. Chem. Phys.* **2005**, *122*, 114105.

(60) Iyengar, S. S. *Theor. Chem. Acc.* in press. DOI: 10.1007/s00214-005-0010-3. Preprint: http://www.indiana.edu/%7Essiweb/papers/TCA.pdf.

(61) Tully, J. C. *Faraday Discuss.* **1998**, *110*, 407−419.

(62) Kapral, R.; Ciccotti, G. *J. Chem. Phys.* **1999**, *110*, 8919.

(63) Horenko, I.; Salzmann, C.; Schmidt, B.; Schutte, C. *J. Chem. Phys.* **2002**, *117*, 11075−11088.

(64) Donoso, A.; Zheng, Y. J.; Martens, C. C. *J. Chem. Phys.* **2003**, *119*, 5010.

(65) Brooksby, C.; Prezhdo, O. V. *Chem. Phys. Lett.* **2001**, *346*, 463−469.

(66) Prezhdo, O. V.; Brooksby, C. *Phys. Rev. Lett.* **2000**, *86*, 3215−3219.

(67) Gindensperger, E.; Meier, C.; Beswick, J. A. *J. Chem. Phys.* **2000**, *113*, 9369.

(68) Hoffman, D. K.; Nayar, N.; Sharafeddin, O. A.; Kouri, D. J. *J. Phys. Chem.* **1991**, *95*, 8299.

(69) Hoffman, D. K.; Kouri, D. J. *J. Phys. Chem.* **1992**, *96*, 9631.

(70) Kouri, D. J.; Huang, Y.; Hoffman, D. K. *Phys. Rev. Lett.* **1995**, *75*, 49−52.

(71) Marchioro, T. L., II; Arnold, M.; Hoffman, D. K.; Zhu, W.; Huang, Y. H.; Kouri, D. J. *Phys. Rev. E* **1994**, *50*, 2320−2330.

(72) Hoffman, D. K.; Arnold, M.; Kouri, D. J. *J. Phys. Chem.* **1992**, *96*, 6539−6545.

(73) Tao, J.; Perdew, J. P.; Staroverov, V. N.; Scuseria, G. E. *Phys. Rev. Lett.* **2003**, *91*, 146401.

(74) Zhao, Y.; Truhlar, D. G. *J. Phys. Chem. A* **2004**, *108*, 6908.

(75) Zhao, Y.; Lynch, B. J.; Truhlar, D. G. *Phys. Chem. Chem. Phys.* **2005**, *7*, 43.

(76) Goedecker, S. *Rev. Mod. Phys.* **1999**, *71*, 1085.

(77) Scuseria, G. E. *J. Phys. Chem. A* **1999**, *103*, 4782.

(78) White, C. A.; Head-Gordon, M. *J. Chem. Phys.* **1994**, *101*, 6593−6605.

(79) Dirac, P. A. M. *The Principles of Quantum Mechanics*, 4th ed.; Oxford University Press: New York, 1958; Vol. 27 of *The International series of monographs on Physics*.

(80) Sakurai, J. J. *Modern Quantum Mechanics;* Addison-Wesley Publishing Company: 1994.

(81) Madelung, E. *Z. Physik* **1926**, *40*, 322−326.

(82) de Broglie, L. *An introduction to the study of wave mechanics;* E. P. Dutton and Company, Inc.: New York, 1930.

(83) Bohm, D. *Quantum Theory;* Prentice Hall Inc.: New York, 1951.

(84) Bohm, D. *Phys. Rev.* **1952**, *85*, 166.

(85) *Bohmian Mechanics: An appraisal;* Cushing, J. T., Fine, A., Goldstein, S., Eds.; Kluwer: Boston, 1996.

(86) Holland, P. R. *The Quantum Theory of Motion;* Cambridge, New York, 1993.

(87) Iyengar, S. S.; Schlegel, H. B.; Voth, G. A. *J. Phys. Chem. A* **2003**, *107*, 7269−7277.

(88) Ehrenfest, P. *Z. Phys.* **1927**, *45*, 455.

(89) Schlegel, H. B.; Iyengar, S. S.; Li, X.; Millam, J. M.; Voth, G. A.; Scuseria, G. E.; Frisch, M. J. *J. Chem. Phys.* **2002**, *117*, 8694.

(90) Iyengar, S. S.; Schlegel, H. B.; Voth, G. A.; Millam, J. M.; Scuseria, G. E.; Frisch, M. J. *Isr. J. Chem.* **2002**, *42*, 191−202.

(91) Rega, N.; Iyengar, S. S.; Voth, G. A.; Schlegel, H. B.; Vreven, T.; Frisch, M. J. *J. Phys. Chem. B* **2004**, *108*, 4210−4220.

(92) Iyengar, S. S.; Frisch, M. J. *J. Chem. Phys.* **2004**, *121*, 5061.

(93) Gibson, D. A.; Ionova, I. V.; Carter, E. A. *Chem. Phys. Lett.* **1995**, *240*, 261.

(94) Tangney, P.; Scandolo, S. *J. Chem. Phys.* **2002**, *116*, 14.

(95) Iyengar, S. S.; Petersen, M. K.; Day, T. J. F.; Burnham, C. J.; Teige, V. E.; Voth, G. A. *J. Chem. Phys.* **2005**, *123*, 084309.

(96) Trotter, M. F. *Proc. Am. Math. Soc.* **1959**, *10*, 545.

(97) Nelson, E. *J. Math. Phys.* **1964**, *5*, 332.

(98) Strang, G. *SIAM J. Numer. Anal.* **1968**, *5*, 506−516.

(99) *Handbook of Mathematical Functions;* Abramowitz, M., Stegan, I. A., Eds.; U.S. GPO: Washington, DC, 1964.

(100) Swope, W. C.; Andersen, H. C.; Berens, P. H.; Wilson, K. R. *J. Chem. Phys.* **1982**, *76*, 637.

(101) Golub, G. H.; van Loan, C. F. *Matrix Computations;* The Johns Hopkins University Press: Baltimore, 1996.

(102) Iyengar, S. S.; Kouri, D. J.; Parker, G. A.; Hoffman, D. K. *Theor. Chem. Acc.* **2000**, *103*, 507−517.

(103) Iyengar, S. S. New Computational Approaches to Quantum Dynamics using "Distributed Approximating Functionals, Ph.D. Thesis, University of Houston, 1998.

(104) Lopreore, C. L.; Wyatt, R. E. *Phys. Rev. Lett.* **1999**, *82*, 5190.

(105) Day, B. K.; Askar, A.; Rabitz, H. A. *J. Chem. Phys.* **1998**, *109*, 8770.

(106) Wyatt, R. E.; Kouri, D. J.; Hoffman, D. K. *J. Chem. Phys.* **2000**, *112*, 10730.

(107) Bittner, E. R.; Wyatt, R. E. *J. Chem. Phys.* **2000**, *113*, 8888.

(108) Wyatt, R. E.; Bittner, E. R. *Comput. Sci. Eng.* **2003**, *5*, 22−30.

(109) Grossman, A.; Morlet, J. *SIAM J. Math. Anal.* **1984**, *15*, 723.

(110) Strang, G. *SIAM Rev.* **1989**, *31*, 613−627.

(111) Daubechies, I. *Ten Lectures in Wavelets;* SIAM: Philadelphia, PA, 1992.

(112) Strang, G.; Nguyen, T. *Wavelets and Filter Banks;* Wellesley-Cambridge Press: 1996.

(113) Strang, G.; Strela, V. *J. Opt. Eng.* **1994**, *33*, 2104−2107.

(114) Arias, T. *Rev. Mod. Phys.* **1999**, *71*, 267−311.

(115) Johnson, B. R.; Modisette, J. P.; Nordlander, P. J.; Kinsey, J. L. *J. Chem. Phys.* **1999**, *110*, 8309−8317.

(116) Bartels, R. H.; Beatty, J. C.; Barsky, B. A. *An Introduction to Splines for use in computer graphics and geometric modeling;* Morgan Kaufman Publishers: Los Altos, CA, 1987.

(117) Carter, S.; Bowman, J. M.; Braams, B. J. *Chem. Phys. Lett.* **2001**, *342*, 636−642.

(118) Iordanov, T.; Billeter, S. R.; Webb, S. P.; Hammes-Schiffer, S. *Chem. Phys. Lett.* **2001**, *27*, 389−397.

(119) Jonsson, T.; Glickman, M. H.; Sun, S. J.; Klinman, J. P. *J. Am. Chem. Soc.* **1996**, *118*, 10319−10320.

(120) Glickman, M. H.; Wiseman, J. S.; Klinman, J. P. *J. Am. Chem. Soc.* **1994**, *116*, 793−794.

(121) Liang, Z.-X.; Klinman, J. *Curr. Opin. Struct. Biol.* **2004**, *14*, 1−8.

(122) Lehnert, N.; Solomon, E. I. *J. Biol. Inorg. Chem.* **2003**, *8*, 294.

(123) Hatcher, E.; Soudackov, A. V.; Hammes-Schiffer, S. *J. Am. Chem. Soc.* **2004**, *126*, 5763−5775.

(124) Olsson, M. H. M.; Siegbahn, P. E. M.; Warshel, A. *J. Am. Chem. Soc.* **2004**, *126*, 2820−2828.

(125) Olsson, M. H. M.; Siegbahn, P. E. M.; Warshel, A. *J. Biol. Inorg. Chem.* **2004**, *9*, 96−99.

(126) Sorensen, D. C. *SIAM J. Matr. Anal. Apps.* **1992**, *13*, 357−385.

(127) Parlett, B. N.; Saad, Y. *Linear Algebra Applications* **1987**, *88/89*, 575−595.

(128) Rahman, A. *Phys. Rev.* **1964**, *136*, A405.

(129) Laasonen, K.; Sprik, M.; Parrinello, M.; Car, R. *J. Chem. Phys.* **1993**, *99*, 9080−9089.

(130) Iyengar, S. S. *J. Chem. Phys.* **2005**, *123*, 084310.

(131) Berens, P. H.; White, S. R.; Wilson, K. R. *J. Chem. Phys.* **1981**, *75*, 515.

(132) Bader, J. S.; Berne, B. J. *J. Chem. Phys.* **1994**, *100*, 8359.

(133) Lawrence, C. P.; Nakayama, A.; Makri, N.; Skinner, J. L. *J. Chem. Phys.* **2004**, *120*, 6621.

(134) Kawaguchi, K. *J. Chem. Phys.* **1988**, *88*, 4186−4189.

(135) Press, W. H.; Teukolsky, S. A.; Vetterling, W. T.; Flannery, B. P. *Numerical Recipes in C;* Cambridge University Press: New York, 1992.

(136) Arfken, G. *Mathematical Methods for Physicists;* Academic Press: New York, 1985.

(137) Li, X.; Iyengar, S. S. Manuscript in preparation.

CT600131G